Effect of Ti on the Corrosion Resistance of Al-Cr-Fe-Mn-Mo-Ni Single and Multi-Phase CCAs

S.B. Inman, Junsoo Han, D.I. Hoyos, S.J. Poon, K.M. Ogle, J.R. Scully

Effect of Ti on the Corrosion Resistance of Al-Cr-Fe-Mn-Mo-Ni Single and Multi-Phase CCAs

S.B. Inman[1,2,3,+], J. Han[1,2,4,5], D.I. Hoyos[6], S.J. Poon[1,6], K.M. Ogle[4], J.R. Scully[1,2]

[1]Department of Materials Science and Engineering, University of Virginia, Charlottesville, VA 22904, USA

[2]Center for Electrochemical Science and Engineering, University of Virginia, Charlottesville, VA 22904, USA

[3]*Presently*, Center for Integrated Nanotechnologies, Sandia National Laboratories, Albuquerque, NM 87185, USA

[4]Chimie ParisTech, PSL Research University, CNRS, Institut de Recherche Chimie Paris (IRCP), F-75005, Paris, France

[5]Sorbonne Université, Laboratoire Interfaces et Systèmes Electrochimiques, F-75005, Paris, France

[6]Department of Physics, University of Virginia, 382 McCormick Road, Charlottesville, VA 22904, USA

[+]Corresponding author: sbi3dk@virginia.edu

Abstract

Five $Al_{0.3}Cr_{0.5}Fe_2Mn_{0.25}Mo_{0.15}Ni_{1.5}Ti_x$ compositionally concentrated alloys were synthesized, forming alloys with an FCC matrix. At Ti concentrations of 5 at. % and above, an $L2_1$ phase enriched in Al, Ti and Ni was present within the FCC matrix. At Ti concentrations of 9.6 at. % Ti and above, a three-phase microstructure containing FCC+$L2_1$+Laves phases was formed, with the Laves third phases enriched in Cr and Mo. Ti(IV) was a prominent constituent in the passive film. Resistance to localized corrosion improved with Ti concentration before reaching an optimal concentration and beginning to decrease, likely due to the formation of new phases.

1.0 Introduction

Ti is a frequent addition to both refractory [1-6] and transition-metal [5-9] based compositionally concentrated alloys (CCAs) providing a wide range of properties including mechanical strength [2, 9-11], low densities [4, 6, 8, 12-15], high-temperature oxidation resistance [7, 16, 17], and aqueous corrosion resistance [2-4, 18].

Strong aqueous corrosion resistance has long been observed for both pure Ti and Ti-based alloys [19-21]. Alloys such as Ti-6Al-4V have shown viability for corrosion resistance in both biological [22-24] and marine [25, 26] environments. The beneficial attributes of Ti to corrosion resistance are attributable to the thermodynamic stability of TiO_2 across a broad range of environments [27, 28]. The oxide is commonly suggested to be amorphous [29, 30], but rutile structures are frequently observed following rapid anodic growth [31, 32] or exposure to increased temperature [27, 33]. Limited presence of hydrogen or hydroxide ions has also been suggested within TiO_2 films, potentially promoting layering behavior [27].

Similar to the case of Ti-dominated alloys, the formation of stable TiO_2 may improve the passivity of alloys for which Ti is a constituent element. For example, the addition of Ti to Fe-Ti binary alloys has been shown to enable the formation of a stable TiO_2 passive film in hydrochloric acid, enabling passivity and improving corrosion resistance [34], however, evaluated compostions were limited to Ti cocencentrations at or above 38 at. %. Therefore, a critical Ti concentration for passivity was not uncovered and further work may be necessary to evaluate the effect of Ti addition at low concentrations. Additionally, the effects of Ti on passivity may be enhanced by co-presence with other constituent alloying elements.

Ti may act as a co-constituent passivator with other passivating elements such as Cr [35]. Like Cr, Ti has been suggested to improve the stability and increase the passive window width of Fe and Al-containing passive films [36, 37], possibly due to the ranges of stable pH for TiO_2 stability being

considerably larger than those of the oxides for Fe, Al, or even Cr [28]. However, unlike the case of the Cr_2O_3-Al_2O_3 system, complete solid solution miscibility is not present between TiO_2 and Cr_2O_3 or Al_2O_3 [38, 39], possibly due to insolubility driven by differences in crystal structure. In addition to phase separated oxides, stochiometric line compounds such as $TiAl_2O_5$ [38], $TiCr_2O_5$, and several other Ti-Cr-O compounds [39] may form on the basis of formation energy [40]; however, there is little experimental evidence indicating Ti-containing complex oxides. The presence of stochiometric line compounds has been theorized to potentially improve passive film stability by improving the potentials and/or pH ranges where otherwise unstable constituent species may be stable [40, 41]. However, there is little definitive evidence as to whether stochiometric line compounds improve corrosion resistance relative to solid solution oxides. Significant overlap in the of cation concentrations-depth profiles in Al-Cr-Ti-V [42], Fe-Cr-Al-Ti [43], and Al-Cr-Fe-Mn-Mo-Ni-Ti [35] passive films suggests that Ti may mix with Al and Cr. However, further work is necessary to evaluate the precise structural, morphological, and chemical nature of such a passive film. Surface and depth profiling with X-ray photoelectron spectroscopy further suggests potential Ti coexistence with Al and/or Cr in additional systems, although enriched levels may vary with depth [4, 8, 43].

The presence of Ti in CCAs, and therefore their passive films, is often suggested to affect corrosion resistance across both single-phase and multi-phase systems [11, 18, 44, 45]. Doping of Ti oxide films has been shown to play a strong effect on oxygen evolution kinetics and corrosion resistance [46], potentially by altering local Ti valence states [47], highlighting the importance of cation miscibility even at small concentrations. Furthermore, the concentration of oxygen vacancies has been tied to the presence, concentration, and/or valence of Ti in the passive film [48-51]. Given the frequent role of oxygen vacancies as charge carriers through the passive film, increasing vacancy concentration can affect passivation and dissolution kinetics [52]. Ti can also improve corrosion resistance as a major constituent in the passive film. For example, when added at a concentration of 30 at. % to equimolar CoCrFeNi, the corrosion

resistance was suggested to improve, most notably in terms of a broader passive range leading to improved pitting resistance in chloride solutions despite the initiation of a Ti-enriched second phase [53].

In some cases, the formation of a new phase outweighs the benefits of Ti additions on corrosion resistance relative to a Ti-free single-phase solid solution CCA. Notably, the addition of Ti promotes phase segregation and decreases overall corrosion resistance . For instance, when Ti is added to the AlCoCuFeNi BCC/B2 crystal structure forms additional FCC and Laves phases with the addition of 16.7 at. % Ti [54]. Similarly, $Al_{0.3}CrFe_{1.5}MnNi_{0.5}$ is a solid solution with a BCC crystal structure but additional FCC, Cr_9Al_{17}, and CrNiFe phases form with the addition of 18.5 at. % Ti [55]. Ti has been further suggested to promote the formation of additional phases of BCC and/or Laves structure across the $Al_2CrFeNiCoCuTi_x$ [56] and $AlCoCrFeNiTi_x$ [57] systems that are locally depleted passivating elements, although an overview of the effects on corrosion resistance was not provided.

While multi-phase alloys frequently have decreased corrosion resistance relative to their single-phase counterparts, the structure and composition of the second phase can influence the magnitude of such effects. Dual-phase CCAs with an FCC matrix containing Ti, Al, and Ni can form an ordered phase such as Huesler ($L2_1$) [58, 59], whereas Ti-free dual-phase CCAs with Al often have comparatively less ordered Al-Ni enriched B2 or BCC phases [60-65]. Joseph et al. observed increasing volume fractions of the ordered $L1_2$ phase in an FCC matrix with increasing Ti/Al ratios in the $Ni_{51}Co_{18}Fe_5Cr_{10}Al_{16-X}Ti_X$ system [66]. Despite frequent adverse corrosion resistance of dual-phase microstructure CCAs [18], corrosion resistance comparable to 316L stainless steel has been observed in FCC CCAs with a Ti-enriched $L2_1$ second phase [35]. Local characterization of passive film chemistry has shown that the passive film contains multiple phases with the composition and size scale informed by the bulk microstructure. The corrosion behavior of multi-phase CCAs is informed by the passivity and corrosion behavior of each individual constituent phase [67]. Thus, it is necessary to ensure both phases contain adequate concentrations of at least at least one stable passivating element (i.e., Cr remains enriched in the FCC matrix and Ti is enriched in the $L2_1$

second phase). In summary, the likelihood of second-phases limitations adds further complexity to the effects of Ti on corrosion behavior.

Xiao et al. [54] compared AlCoCuFeNi and AlCrCoCuFeNi CCAs with and without equimolar Ti additions. For both alloy systems, the only second phase present in the Ti-free CCAs was disordered BCC. Ti additions to both alloys introduced a Laves phase as well as stabilized an ordered B2 phase. The Ti-containing alloys were suggested to have inferior corrosion resistance in chloride solution on the basis of corrosion potential, corrosion current density, and polarization resistance relative to the Ti-free alloys of otherwise equal composition. However, the effect of Ti on passivity and film breakdown in each phase were not explored, and thus possible passivity benefits of Ti were not addressed. Qi et al. [9] observed improved passive and corrosion current densities with the addition of Al and Ti to CoCrFeNi, but the pitting potential decreased due to the stabilization of the B2 phase and $L1_2$ nanoprecipitates within the FCC matrix. Significant Al, Cr, and Ti presence was shown in the passive film, suggesting Ti plays an active role in improving passivity and is likely enriched relative to bulk composition. However, precise surface cation fractions were not provided. Although the microstructural refinement affected corrosion behavior, it is unclear to what degree Ti is responsible for the changes given the parallel addition of Al.

Ti clearly can have a key role in the passivity and corrosion resistance of CCAs. However, the prominent effects on microstructure, most frequently through the stabilization of often undesirable phases, in many of the examples above have undesirable effects on overall corrosion resistance. Despite the ability of Ti to form a stable passive film over a single phase, it could possibly decrease corrosion resistance relative to a single-phase solid solution with lower concentrations of or no Ti, particularly if a phase depleted in passivating elements is formed. While such effects of Ti are well-studied, studies evaluating the behavior of alloys with a systematic range of Ti concentrations across both single-phase and multi-phase regions are comparatively less frequent, and often evaluated on coatings as opposed to bulk samples [56, 59]. This highlights a need to further evaluate the effect of minor Ti additions in across

a wide range of compositions, particularly the possibility of forming a TiO_2-containing passive film while avoiding the formation of detrimental phases depleted in passivating elements. Moreover, it is of interest to learn whether low Ti content can form a protective passive film aided by a second alloying element. Such findings would provide a basis to optimize Ti concentration for a given CCA system.

This study explores the effects of Ti concentration on a series of $Al_{0.3}Cr_{0.5}Fe_2Mn_{0.25}Mo_{0.15}Ni_{1.5}Ti_x$ CCAs with Ti concentrations between 0.0 and 13.0 at. % Ti with the goal of providing insight on Ti optimization for corrosion resistance. The phases present, second phase morphology, and composition of each phase were characterized with combinations of X-ray diffraction (XRD), scanning electron microscopy (SEM), and energy dispersive spectroscopy (EDS). Special attention was dedicated into checking whether any phases were depleted in passivating elements. The corrosion behavior was then evaluated with combinations of potentiodynamic polarization and electrochemical impedance spectroscopy (EIS), while trends in the presence and composition of Ti in the passive film were evaluated with X-ray photoelectron spectroscopy (XPS). The findings were used to uncover the molecular identity of the passive degree of enrichment of Ti(IV) in the passive films, the nature of multi-cation oxide formation, and to inform compositional optimization of Ti in the $Al_{0.3}Cr_{0.5}Fe_2Mn_{0.25}Mo_{0.15}Ni_{1.5}Ti_x$ alloy family.

2.0 Experimental Methods

2.1 Alloy Synthesis and Microstructural Characterization

Five CCAs in the $Al_{0.3}Cr_{0.5}Fe_2Mn_{0.25}Mo_{0.15}Ni_{1.5}Ti_x$ (x = 0, 0.15, 0.3, 0.5, 0.7) system with compositions listed in Table I were synthesized from high-purity elements (Cr > 99.2%, all other metals > 99.9%) and arc melted into button samples 1 cm in diameter. Samples were flipped and remelted five times to ensure homogeneity before encapsulation in quartz tubing under Ar. A 6-hour homogenization heat treatment at 1070 ˚C was applied, followed by quenching in water. Proposed compositions were first modeled with an isopleth diagram developed with CALPHAD techniques using ThermoCalc software operating with the

TCHEA3 database. Compositions and heat treatments were selected with the goal of reducing cost and density, ensuring an adequate concentration of passivating elements, and targeting a second-phase reinforced FCC microstructure using methods described elsewhere [68]. The compositions of Mn [69] and Mo [70] were guided by previous work in alloying systems varying the concentrations of each respective elements. Accuracy of targeted compositions within 0.5 at. % for each element were verified by EDS mapping of selected alloys following homogenization described further below.

Following homogenization, sample surfaces were mechanically ground through 1200 grit paper, and further polished through 1 µm diamond suspension in the case of microstructural and surface analysis. Microstructures were identified via XRD with an PANalytical Empyrean Diffractometer™ operating with Cu Kα X-rays (1468.7 eV) and a scan rate of 0.15 ˚/s. Additionally, microstructures were imaged with a FEI Quanta 650™ scanning electron microscope operating in back scattered electron (BSE) mode at an accelerating voltage of 15 keV, a probe size of approximately 5 nm, and a working distance of approximately 10 mm. Partitioning of elements across phases was characterized with EDS point scans and analyzed with Oxford Instruments Aztec™ software.

2.2 Electrochemical Characterization

A conventional three-electrode cell regulated by a Gamry Instrument Reference 600+™ potentiostat was used for electrochemical characterization of the corrosion behavior. The CCA samples deployed as the working electrode had an exposure area[1] of 0.784 cm^2 defined by a rubber O-ring. A platinum mesh counter electrode and a saturated calomel reference electrode (SCE, 0.241 V vs. SHE) were utilized. 0.01 M NaCl with a natural pH of approximately 5.75 was used as the electrolyte for all experiments to examine the passive region. Select experiments were performed in 0.001, 0.1, and 1 M

[1] For tests requiring ex-situ characterization that prohibited the use of epoxy mounting (polarization with subsequent pit imaging, potentiostatic oxide growth with subsequent XPS characterization), a smaller exposure area of 0.1 cm^2 was used. The change is accounted for with area-normalized current and impedance parameters.

NaCl with a natural pH ranging between 5.5 and 6. $N_{2(g)}$ was continually bubbled during the experiments to minimize the effects of dissolved oxygen. All electrochemical experiments were repeated in triplicte. Each synthesized CCA was compared to commercially produced (North American Steel) 316L to ensure reproducibility.

First, potentiodynamic polarization was used to characterize the formation and breakdown behavior of the passive film. To minimize the effects of the air-formed oxide, a cathodic potential of -1.3 V_{SCE} was applied for 600 s. The potential was then swept from -1.3 to 0.8 V_{SCE} at a rate of 0.5 mV/s before a reverse scan from 0.8 to -1.3 V_{SCE}. Additionally, the impedance of the film, specifically the imaginary component, was monitored in-situ during the polarization by applying three AC cycles at every 5 mV increase in applied potential. These were conducted at a frequency of 1 Hz and an amplitude of 20 mV_{RMS}. While trends in passive film thickness were tracked using previously described relationships [71-73], The absolute thickness was not calculated due to uncertainty over oxide identity and dielectric constant. The potential range was selected to ensure a sufficient driving force for the reduction of Cr-dominated air-formed oxide[2] (predicted to reduce at potentials more negative than -1.30 V_{SCE} in pH ~5.75 by E-pH diagrams [28]) as well as to ensure sufficient driving force for the subsequent formation of Al_2O_3, TiO_2, and Cr_2O_3 (which are suggested by E-pH diagrams to form at potentials more positive than -2.14, -1.87, and -1.30 V_{SCE}, respectively, on their respective pure metals in pH ~5.75 conditions [28]). An additional trial was repeated and terminated upon the anodic current density exceeding 10^{-5} A/cm^2 and then imaged via SEM to identify pit initiation sites and morphology.

[2] While more negative potentials are necessary to reduce Al_2O_3 or TiO_2 on pure Al or Ti, respectively, previous work in the alloy system has shown a -1.3 V_{SCE} potential to be sufficient to reduce the air-formed oxide [35]. More negative potentials are not used to avoid excessive cathodic reaction rates beyond those necessary to reduce the air-formed oxide. The lack of an air-formed oxide is verified for the evaluated alloy series via in-situ impedance measurements described above.

For potentiodynamic polarization of the Ti-6.0 alloy, elemental dissolution rates were tracked in-situ via Inductively Coupled Plasma Atomic Emission Spectroelectrochemistry (AESEC). A Horiba Jobin Yvon Ultima system described elsewhere [74] was utilized with a 0.5 m polychromator. Mo signal was obtained with a monochromator with a focal length of 1.0 m to improve resolution. To increase dissolution rates above the elemental detection limits, a more aggressive 0.1 M NaCl solution adjusted to a pH of 4 with concentrated HCl was used. Additionally, the $N_{2(g)}$ bubbling and cathodic pre-treatments were bypassed. Elemental intensities at characteristic wavelengths (I_M) were converted dissolution rates (v_M) with f and A referring to the flow rate and area, respectively. Equivalent dissolution rates were then converted to equivalent current densities (j_M) via Faraday's law with z_M, F, and M_M referring to the elemental charge, Faraday's constant, and the molar mass, respectively. To differentiate elemental dissolution rates without the effects of the composition of each element (X_M), equivalent current densities were normalized (j'_M) relative to Fe, the primary constituent element of Ti-6.0. A more thorough discussion of the calculation methodology is provided elsewhere [74].

$$v_M = \frac{f I_M}{A} \quad (1)$$

$$j_M = \frac{z_M F v_M}{M_M} \quad (2)$$

$$j'_M = \frac{j_M z_{Fe} X_{Fe}}{z_M X_M} \quad (3)$$

The corrosion behavior of the CCAs with air-formed oxides was also evaluated. First, open circuit potential (OCP) of the air-formed oxide was monitored for 1800 s. The impedance was then characterized with EIS at a frequency range from 100 kHz to 1 mHz with 5 points measured per decade and an AC sinusoidal amplitude of 20 mV_{RMS}. Following EIS, the alloy was polarized from -0.1 V relative to the established OCP to 0.8 V_{SCE} at a 0.5 mV/s scan rate in the upward direction and then polarized from 0.8 to -1.3 V_{SCE} with the reverse scan described above.

Finally, to characterize the composition and corrosion behavior of a stable passive film formed electrochemically, a third procedure was utilized. The CCA was first exposed to the -1.3 V_{SCE} cathodic treatment described above for 600 s to reduce the effects of the air-formed oxide. A -0.25 V_{SCE} potentiostaic hold, a potential determined to be within the passive range of all evaluated CCAs evaluated during initial polarization testing, was then applied for 40 ks, during which the current density and in-situ impedance (1 Hz, 20 mV_{RMS}) were monitored. The oxide was then characterized with EIS at -0.25 V_{SCE}, otherwise with the same parameters described above (100 kHz to 1 mHz, 20 mV_{RMS}, 5 points/decade). Finally, OCP of the alloy was monitored for 30 minutes.[3]

2.3 Chemical Analysis of Passive Film

Three CCAs with Ti concentrations of 0, 6.0, and 9.6 at. % and FCC, FCC + $L2_1$, and FCC + $L2_1$ + Laves microstructures, respectively, were selected to evaluate the effect of Ti content on passive film composition and chemistry. A passive film was grown at -0.25 V_{SCE} for 40 ks and characterized with EIS using the procedure described above before transfer under $N_{2(g)}$ to a PHI VersaProbe III™ XPS system. High-resolution spectra were collected over the C1s, O1s, Al 2p, Cr $2p_{3/2}$, Fe $2p_{1/2}$[4], Mn $2p_{1/2}$, Mo 3d, Ni $2p_{3/2}$, and Ti $2p_{3/2}$ (when present) core series with Al Kα X-rays (1486.3eV), a 100 µm spot size, a 26 eV pass energy and a 0.05 eV step size. A Shirly background substitution was first used to remove background noise before fitting of features to asymmetric Doniach-Sunjic peaks for metallic or zero-valance solute trapped feature or symmetric Voight peaks for oxidized cations. Peaks were fit to reference spectra obtained elsewhere from combinations of binding energy, width, amplitude, and multiplet splitting [75-78]. Following fitting of the high-resolution spectra, the intensities (I_X) of all features attributable to oxidized features (non-zero valance) were summed. The intensities were then normalized to the relative

[3] For XPS surface characterization, the final OCP step was bypassed to minimize exposure prior to surface characterization.

[4] Due to overlap with Ni auger peaks, traditionally utilized Fe $2p_{3/2}$ and Mn $2p_{3/2}$ core series were eschewed in favor of the $2p_{1/2}$ series.

sensitivity factors (RSF) obtained from PHI Mulitipak™ software for each series and divided over the cumulative intensity for each element to obtain the surface cation fraction (X^S) as shown below.

$$X_A^S = \frac{\frac{I_A}{RSF_A}}{\Sigma \frac{\mathrm{I_X}}{RSF_X}} \quad (4)$$

3.0 Results

3.1 CCA Microstructure

XRD patterns shown in Figure 1 indicate the presence of single phase over low Ti concentrations with second and third phase formation at higher Ti concentrations. All CCAs are suggested to contain the FCC phase. Beyond 6.0 at. % Ti, a second BCC-like phase that has been identified elsewhere as $L2_1$ is indexable [68]. Finally, at concentrations at 9.6 at. % Ti and above, a third phase is present. Although the exact structure cannot be indexed due to low intensity, the many peaks present suggest likely ordering and/or the presence of a non-cubic lattice. The isopleth diagram for the $Al_{0.3}Cr_{0.5}Fe_2Mn_{0.25}Mo_{0.15}Ni_{1.5}Ti_x$ system shown in Figure 2 suggests the presence of a single-phase FCC microstructure while indicating the stability of C14 Laves beyond 8 at. % Ti, suggesting a likely Laves structure for the third phase found in Ti-9.6 and Ti-13.0. The diagram further suggests increasing volume fractions of the $L2_1$ and Laves phases with increasing Ti concentrations. Table II highlights that while CALPHAD correctly predicts that single-phase microstructures do not occur at higher Ti concentrations, the Ti concentrations necessary to form additional phases are not predicted correctly. Notably, $L2_1$ presence is not predicted by the isopleth diagram at Ti concentrations below 12 at. % Ti, indicating possible metastable presence in Ti-6.0 and Ti-9.6. Predictions for the presence of multi-phase microstructures are using previously established [13, 79, 80] thermodynamics-based indicators are further evaluated in the supplementary information section.

The presence of new phases with increasing Ti concentration is additionally confirmed by the BSE micrographs shown in Figure 3. For the 6.0 at. % Ti CCA, the alloy $L2_1$ second phase regions on the order

of single-μm with a low volume fraction. In the two high-Ti CCAs, larger regions of approximately 10 μm that alternate between single-μm $L2_1$ and Laves phase regions are present.

EDS mapping and point scans of selected CCAs shown in Figure 4 and Table III, respectively, reveal which elements are enriched in each phase. In Ti-6.0, the FCC matrix is enriched in Fe, Mn, Mo, and Cr relative to the bulk composition shown in Table I. The $L2_1$ phase is enriched in Al, Ni, and Ti. Furthermore, the area fractions obtained via ImageJ threshold analysis indicate the phase fraction of the FCC matrix is significantly higher than that of the $L2_1$ phase.

Ti-13.0 has a three-phase microstructure with an additional Laves phase that is enriched in Cr, Fe, and Mo relative to the bulk composition. The FCC matrix is enriched in Fe, Cr, and Mn relative to bulk alloy composition, but unlike Ti-6.0, is not enriched in Mo. The $L2_1$ phase was enriched in Al, Ni, and Ti. Both the $L2_1$ second phase and Laves third phase have similar phase fractions, and are both present at higher fractions than the $L2_1$ phase of the lower Ti-concentration CCAs such as Ti-6.0. For both Ti-6.0 and Ti-13.0, every phase is enriched in at least one stable passivating element, either Cr or Ti, relative to the bulk alloy composition (Table I). Point scans of Ti-0 and global alloy compositions obtained from the mapping of Ti-6.0 and Ti-9.6 suggest the true composition is within 0.5 at. % of the initial targeted compositions, suggesting that there was no significant material loss during arc-melting.

3.2 Polarization of CCAs Following Cathodic Pre-treatment

Potentiodynamic polarization was used to characterize the electrochemical behavior and corrosion resistance of the CCAs. An E-log(i) plot obtained during polarization of the series of CCAs that were first cathodically pre-treated to evaluate film formation on a reduced or minimized oxide metal surface is shown in Figure 5. Additionally, in-situ single frequency impedance (-Z") measurements in the oxide capacitance frequency range are also shown along with key parameters tabulated in Table IV and shown in Figure 6. Spontaneous passivity is shown for all evaluated CCAs in the dilute chloride solution,

which is expected given the ability of both Al and Ti to form spontaneous passive films below the reversible hydrogen electrode potential under neutral conditions as indicated by the horizontal lines at each metal's oxidation/reduction potential [28]. For all alloys, -Z" immediately begins to rise with potential, suggesting the passive film increases in thickness directly proportionality to -Z". No clear critical current densities are discernible. which, along with the continually increasing -Z" magnitudes, suggest that no active to passive transitions were observed.

No clear trends between E_{corr} and Ti concentration were suggested. Ti-13.0 shows a significantly higher E_{corr}, but the deviations are not suggested to be statistically significant and could arise from variations in oxygen reduction caused by incomplete dissolved oxygen purging during $N_{2(g)}$ bubbling. High E_{corr} values could additionally be influenced by incomplete reduction of air-formed oxide, particularly given the standard reduction potential of Ti being below the -1.3 V_{SCE} potential used for cathodic reduction. However, the low -Z" values for all alloys at -1.3 V_{SCE} suggest complete or near-complete oxide reduction or minimization, as opposed to the comparatively much higher values of the air-formed oxides characterized in section 3.3 (Figure 10). Alternatively, it is possible that limited oxide growth occurred between the beginning of the polarization process and E_{corr} given the stability of Al, Ti, and Cr passive species over the potential range. Between 0 and 9.6 at. % Ti, i_{pass} decreases with Ti concentration, signifying the formation of a thicker and/or more protective passive film. Between 9.6 and 13 at. % Ti, i_{pass} rises, although not at a significant level. Pitting was the dominant breakdown mechanism for all CCAs with some crevice corrosion also observed. Intermittent increases in current density along with corresponding decreases in -Z" suggest metastable pitting that repassivated prior to complete film breakdown. E_{pit} was highest for Ti-6.0 while Ti-0 has the lowest E_{pit}. The lack of a well-defined vertical passive range for Ti-0 suggests a weak or non-protective passive film, leading to both a low E_{pit} and a high i_{pass} that continues to rise as potential is scanned upwards. Notably, E_{pit} for Ti-6.0 exceeds the potential for which Cr_2O_3 is stable on pure Cr before transpassivity. The extension of the passive range to such potentials indicates a partially

protective oxide remains despite the possibility of Cr(VI) dissolution, likely due the stability of Al- and Ti-containing passive species [35]. While no trends were present between Ti concentration and -Z" at -0.25 V_{SCE}, the potential at which i_{pass} was defined, Ti-6.0 reached the highest -Z" magnitude of all tested CCAs, suggesting the formation of a thicker passive film during polarization. The increase is attributable to the higher E_{pit} allowing for increased time and/or driving force for film formation at increased potentials where the films of other CCAs had already broken down. Finally, E_{rep} follows similar trends as E_{pit}, with the Ti-0 having the minimum value and Ti-6.0 having the maximum value[5].

Potentiodynamic polarization was also evaluated for both the best-performing and worst performing CCAs (Ti-6.0 and Ti-0) across a broad range of NaCl concentrations. Representative E-log(i) curves alongside trends in E_{pit} as a function of Cl^- concentration are shown in Figure 7. Increasing E_{pit} values from Ti-0 to Ti-6.0, indicating Ti addition improves the local corrosion resistance across all evaluated NaCl concentrations. The pitting potentials decreases at similar NaCl concentrations for both CCAs. Current densities for Ti-0 generally increase with NaCl concentration, while such trends were less prominent for Ti-6.0.

Elemental dissolution equivalent current densities obtained during potentiodynamic polarization of Ti-6.0 in 0.1 M NaCl adjusted to pH 4 are shown in Figure 8. Elemental current densities are first normalized (j_M') from the Eq. 3. The equivalent Al dissolution current density is not presented due to high noise level. All elemental dissolution rates are below the detection limit until the potential sweep reaches a transpassive domain near 0.23 V_{SCE}. Thus, although significant Ti dissolution is not observed, trends in dissolution rates with regards to potentials within the passive range and quantitative comparisons made to dissolution rates of other elements cannot be accurately assessed due to the detection limit. Notably,

[5] Downward scans are not shown in Figure 5 to ensure data visibility. The tabulated E_{rep} values were obtained at the crossover point, or the potential at which the downward scan current density is less than that of the upward anodic scan at the same potential.

significant Cr dissolution, presumably due to the formation of Cr(VI), is observed in the transpassive domain. Additionally, it may be concluded that equivalent current densities at the potentials for which active dissolution occurs are not suggested to be proportional to the composition of either phase. Thus, preferential congruent dissolution of either phase, which would lead to increased dissolution of certain elements enriched in the phase, likely at rates beyond the detection limits, is not suggested to be present. Therefore, each phase may be considered protected. In the transpassive domain, the normalized Mo dissolution current density is below the congruent level, indicating Mo retention [81] in this potential domain. Mn also showed a slightly low dissolution rate than the congruent dissolution level, similar to other multi-principal element alloys in the same electrolyte [82].

Micrographs of the CCA surfaces following polarization of the cathodically pre-treated surfaces in 0.01 M NaCl are shown in Figure 9. The significantly greater density of features relative to the non-polarized surfaces (Figure 3) indicates that while limited porosity may be present, the majority of feature may be attributable to pit formation. For the single-phase CCAs (Ti-0 and Ti-3.1), pitting appears to initiate at random locations, whereas for the multi-phase CCAs (Ti-6.0, Ti-9.6, and Ti-13.0), pitting preferentially occurs at or near phase interfaces. None of the phases is suggested to be preferentially dissolved, however, the polarization was terminated prior to significant pit propagation.

3.3 Characterization of CCAs with Air-Formed Oxides

Polarization and in-situ -Z" measurements were also evaluated for a CCA series initiating slightly below the OCP to characterize the corrosion behavior of the CCAs without reduction of the air-formed oxide films. These are shown in Figure 10 and summarized in Table V. Similar to the case of the oxide formed on the reduced metal surface, polarization of the air-formed solution-exposed oxides shows the lowest values of both E_{pit} and E_{rep} for Ti-0, suggesting inferior corrosion resistance. Additionally, Ti-6.0 has the highest E_{corr} value while Ti-0 has the lowest, although other CCAs have E_{corr} values within the statistical

scatter of Ti-0. All three parameters are suggested to increase with Ti concentration between 0 and 6 at. % Ti. However, such trends do not extend to Ti-9.6, the first CCA to have three phases. Despite increasing E_{corr}, E_{pit}, and E_{rep} values from Ti-9.6 to Ti-13.0, Ti-6.0 remains the only tested CCAs to exceed 316L in any of the evaluated parameters, suggesting all the other CCAs have inferior corrosion resistance to 316L.

CCAs with air-formed oxides were also characterized with EIS to characterize the passive film prior to polarization. A representative Bode plot along with tabulated fit parameters for a Randles circuit modified to include a constant phase element (CPE) are shown in Figure 11 and Table VI, respectively. Impedance (Z) at a given frequency (f) may be calculated from equivalent circuit parameters including the polarization resistance (R_p), solution resistance (R_s), CPE coefficient (α), and admittance constant (Y_0). The R_P term describes transport O^{2-} anion and metal cations as the charged species and compensating defects to preserve electroneutrality (e.g., electrons, holes) affect interfacial electrochemical reaction rates. The CPE contains information on the dielectric and physical attributes of oxide in stratified layers [83]. The simplified circuit fits the behavior to a single time constant dominated for which resistance is dominated by the R_p term, allowing for an overall sense of oxide protectiveness.

High α values for all CCAs indicate that the fits are representative of near-capacitive behavior usually associated with behavior approximately by planar conformal oxides [72]. Generally, it is found that R_p increases with Ti concentration for air formed oxides exposed to solution, with trends in the fit spectra validated by similar trends in the low-frequency impedance modulus of supplemental runs. Increasing R_p magnitudes suggest the formation of a more protective passive films with increasing Ti concentration. It is notable that the presence of a multi-phase microstructures does not lower R_P as OCP is well below E_{pit}, and thus, R_P at OCP is not reflective of local corrosion. None of the phase angle plots suggests the presence of multiple CPEs, however, the change in shape of the Nyquist plots (not shown) at low-frequencies indicate several time constants with possible mass transfer-controlled kinetic processes, particularly in the case of Ti-3.1. When passivity is studied, such mass transport kinetics are usually attributable to

transport by migration and diffusion through the through the passive film [83]. Given the variance in low-frequency impedance magnitude values between runs, uncertainty remains in quantitative R_p comparisons such as the observed for decrease for Ti-3.1 relative to Ti-0.

3.4 Growth and Electrochemical Properties of Passive Film Formed in Electrolyte Solution

The formation of the passive film from a reduced metal surface was also evaluated. Figure 12 shows current density and -Z" measurements obtained during exposure of cathodically pre-treated surfaces to an applied potential of -0.25 V_{SCE}. In addition to being above the oxide formation potentials of Al, Cr, Ti, and Mo in pH ~5.75 conditions [28], the potential is within the passive range of all evaluated CCAs previously determined with potentiodynamic polarization (Figure 5). For all CCAs, the current density initially decays for the first 10^3 seconds, suggesting the formation of a stable passive film. Between 10^3 and 10^4 seconds, the sign of the current density changes to cathodic for all CCAs and the magnitude decreases below the levels characteristic of residual O_2 reduction. -Z" generally increases for at least 10^4 seconds, indicating the formation of a thicker passive film, before leveling out. No clear trends are present regarding the film growth kinetics with Ti concentration, with deviations between CCAs potentially obscured within statistical scatter. Nonetheless thickening protective passive films are suggested for all alloys under the conditions testing, indicating the alloys remained passive.

Following film growth, the CCAs were characterized by a full EIS spectrum at the growth potential. Selected spectra fit to the Randles circuit described above are shown in Figure 13. Tabulated fit parameters are shown in Table VII. All fits indicate an α value above 0.75, suggesting capacitive behavior indicative of passive film formation. All of the CCAs have R_p values higher than that of 316L. No abrupt drops for multi-phase CCAs were observed relative to the single-phase CCAs and differences between the individual CCAs are not statistically significant. Thus, unlike the case of the air-formed oxides, R_p is not suggested to increase with Ti concentrations.

3.5 Composition and Chemical Properties of Passive Film Formed in Electrolyte Solution

The composition of the passive film was analyzed with XPS for a low- (Ti-0), medium- (Ti-6.0), and high-Ti (Ti-9.6) CCA with FCC, FCC+$L2_1$, and FCC+$L2_1$+Laves microstructures, respectively, with fit spectra for passivating elements Al, Cr, and Ti are shown in Figure 14. The presence of passive species for Al and Ti, elements enriched in the $L2_1$ phase, alongside Cr, which is enriched in the FCC and Laves phases, suggest passivity is present over both phases. Ti spectra contain features attributable to Ti(IV) oxide for both Ti-9.6 but not for Ti-6.0, with Ti^0 (unoxidized metallic signal) is observed for Ti-9.6[6]. Signal attributable to Al^0, Al(III), and the Cr 3s core series is observed for all three CCAs. All Cr spectra showed features attributable to high concentrations of Cr(III) hydroxide with Cr(III) oxide and unoxidized Cr^0 also present. Additionally possible $FeCr_2O_4$ spinel presence is indicated for the Ti-0 and Ti-6.0 passive films by the Cr and Fe (not shown) spectra, but not for that of Ti-9.6. Frequently observed peaks attributable to unoxidized metallic features substantiate that the oxide film is thin in all alloys.

Surface cation fractions are shown in Figure 15 and tabulated in Table VIII. Cr(III) is enriched, mainly in the form of Cr(III) hydroxide, relative to its bulk composition in all three alloys, and is the largest constituent cation at the surface in two of the three CCAs. For the two Ti-containing CCAs, Ti(IV) oxide is also enriched relative to its bulk composition. Despite the increase in overall Ti composition from Ti-6.0 to Ti-9.6, the Ti(IV) concentration at the surface is suggested to decrease. Al(III) is sparingly present in all three films, but is only enriched relative to bulk composition in the Ti-6.0 passive film. The distribution of Al in the passive film may likewise be affected by its preferential partitioning to the $L2_1$ phase and away from both the FCC and Laves phases where it is depleted. Significant Mo(VI) presence is also suggested as

[6] The evaluated binding energy range for the high-resolution $Ti2p_{3/2}$ scan of Ti-6.0, which does not characteristic binding energies of Ti^0, was defined by initial high-intensity survey scans (not-shown), where no signal was observed in the characteristic Ti^0 binding energy range.

well as low concentrations of Fe(II)/Fe(III), Mn(II), and Ni(II). However, no clear trends are present with Ti concentration.

Discussion

4.1 Thermodynamics of Passive Film Formation

All evaluated CCAs are suggested to form protective passive films as evidenced by combinations of broad passive ranges and increasing -Z" values observed during potentiodynamic polarization (Figures 5, 10), high R_P magnitudes determined by EIS (Figures 11, 13, Tables V, VI), and increasing -Z" values accompanied by decreasing current densities during potentiostatic oxide growth (Figure 12). Such behavior is observed for both single-phase CCAs as well as those containing additional $L2_1$ and/or Laves phases. The maintenance of passivity, despite second phase formation, distinguishes this CCA class from many multi-phase CCAs. It is enabled by ensuring both phases have at least one passivating element enriched in each phase (e.g. Cr in the FCC matrix and Laves, Ti in the $L2_1$) presumably up to some critical concentration or boosted in some way like a third element effect. Local enrichment of passivating elements is necessary given the expectation a passive film with a unique composition is formed over each phase [67].

All of the protective oxide species discussed herein are predicted to be thermodynamically stable when considering exposure of pure Al, Cr, Fe, and Ti to -0.25 V_{SCE} in pH ~5.75 chloride solution, the environment used for potentiostatic oxide growth [28]. The potentials for localized breakdown prior to increases in current density as well as non-zero -Z" values indicate the presence of a stable passive film beyond the range of Cr(III) stability in the form of Cr_2O_3 (Figures 5, 10). This suggests that oxide stability is substantial due to Al and Ti alloying and due to subsequent Al(III) and/or Ti(IV) participation in passivation despite their low concentrations in the bulk alloy. Equivalent dissolution current densities obtained for all elements within the transpassive range of potentiodynamic polarization were below the detection limit

(Figure 8), despite the predicted dissolution for Al, Fe, Mn, Mo, and Ni in pH 4 environments [28]. Thus, the passive films of the CCAs are defined by the contributions of multiple cations located within the passive film.

While convex hull and E-pH diagrams are effective in predicting whether the formation of an oxide film will be thermodynamically favorable, they are insufficient in predicting which oxides will be comparatively more prevalent based on kinetic considerations or in specifying the critical concentration of the element, the effects of the electrolyte, and the impact of pH. The free energy of formation (ΔG°) may also be used to compare the driving force for passivation among multiple species. For example, ΔG° of Al_2O_3, Cr_2O_3, and TiO_2, (-1690 kJ/mol [84], -1050 kJ/mol [85], and -970 kJ/mol [84], respectively) are all more negative on a per molecule basis than that of Fe_2O_3 (-742 kJ/mol [84]). Furthermore, ΔG° of TiO_2 is more negative than Cr_2O_3 and comparable to Al_2O_3 when considered on a per atom basis. More negative ΔG° values indicate a higher driving force for passivation, leading to Al(III), Ti(IV) and Cr(III) enrichment that is often observed relative to bulk concentration while Fe(II)/Fe(III) is depleted for all CCAs (Figure 15). Therefore, while E-pH behavior for a given electrolyte may indicate possible passive species stability, additional information such as ΔG° and other kinetic considerations are needed to predict enrichment relative to bulk concentration. For example, possible $FeCr_2O_4$ formation suggested by XPS fitting (Figure 14) may be driven by the more negative ΔG° (-1340 kJ/mol [85]) as well as the extended 40 ks exposure, which has been suggested to lead to the transition to comparatively more thermodynamically stable species in Ni-Cr-Mo alloys [86].

Figure 16 surveys a range of passive species collected using density functional theory calculations with methodologies developed elsewhere [87, 88], illustrating the generally lower free energies of the species containing Al, Cr, or Ti relative to other less-enriched cations. Such ΔG° values shown also indicate the most thermodynamically stable oxide species for a given element. For Ti, the most energetically stable oxide is suggested to be TiO_2 whereas the Cr species with the lowest formation energy on a per atom basis

is Cr_2O_3. Both Cr(III) and Ti(IV) are suggested to be the most stable valences in the passive film by XPS fitting (Figure 14), although $Cr(OH)_3$ is suggested to be considerably more present due to the local availability of hydroxide anions.

In addition to favorable stoichiometric single element oxides and the possibility of long-range ordered oxide formation, the possibility of oxide mixing may further contribute to stability in the passive film. For example, Wang et al. suggested the free energy of mixing (ΔG_{mix}) for Fe_2O_3 and Cr_2O_3 may further promote mixed oxide stability during aqueous passivation of CCAs [89]. However, such effects may be less prominent for Ti(IV) given the different structures and valence states suggested for the oxides (Figure 14) as well as the large two-phase regions (i.e. phase separation) present in the Cr_2O_3-TiO_2 [90] and Al_2O_3-TiO_2 [91] phase diagrams. While many stable complex oxides are present in the phase diagrams at room temperature, including Al_2TiO_5, $Ti_4Cr_2O_{11}$, $Ti_5Cr_2O_{11}$, $Ti_6Cr_2O_{11}$, $Ti_7Cr_2O_{11}$, and more, although none has been experimentally confirmed to form in aqueous environments.

4.2 Kinetics of Passive Film Formation

While thermodynamic factors help to ensure a sufficient driving force is present for passivation of a given element, comparative enrichment levels between elements may also be affected by kinetic considerations, particularly given the multiple cations often present within the passive films of CCAs [41]. Such factors may limit the enrichment of slow-passivating species in favor of comparatively more rapid passivators and/or lead to the formation of multiple layers within the passive film with enriched cations influenced both by passivation kinetics in addition to thermodynamic miscibility, leading to possible discrepancies in the passive film chemistry from that which may be predicted by ΔG^0 values alone.

Work in the Fe-Cr-Al-Ti system has shown that quaternary alloys with higher Ti concentrations may have multiple oxide layers form whereas alloys with less Ti may have the majority of Ti(IV) dissolved in an unlayered solid solution oxide [43]. Such layering may be influenced by the limited solubility of Ti(IV)

species in Fe(II)/Fe(III) or Cr(III) dominated passive films. In both the Fe-Cr-Al-Ti [43] and Al-Cr-Fe-Mn-Mo-Ni-Ti [35] systems, Ti is suggested to be more enriched in inner layers closer to the metal-oxide interface than other passivators such as Cr(III). Notably, Ti is often enriched at similar depths as Al, possibly allowing the stabilization Al(III) either through thermodynamic mixing effects and/or stable Ti(IV) enriched layers protecting metastable Al(III) that may otherwise chemically dissolve in the absence of Ti. While inner-oxide enriched Ti(IV) may not be observed to the same degree by XPS it could still contribute to overall passivity, leading to the high impedance moduli and low i_{pass} magnitudes (Figures 5, 6, 12, Tables IV, VII) of Ti-rich CCAs such as Ti-13.0. Possible inner-layer enrichment of Ti in Ti-9.6, which showed a lower surface cation fraction than Ti-6.0 (Figure 15, Table VIII), could be verified with additional depth profiling work.

In addition to the global composition, the ability to passivate may be considered on a basis of the composition of constituent phases. Previous work on Ti-6.0 has shown that the passive film formed over the FCC phase has considerably higher Cr surface cation fractions in the passive film, while the film formed over the $L2_1$ phase has higher concentrations of Al, Ni, and Ti [67]. The local compositions within the passive follow trends with enriched elements in individual microstructural phases relative to global alloy composition (Table II). Therefore, although not characterized, the Laves phase formed in Ti-9.6 and Ti-13.0 likely also has Cr and Mo enriched over it.

4.3 Microstructural Effects on Corrosion Behavior

CCAs with higher Ti concentrations generally demonstrate superior passivity. suggesting that the $L2_1$ and/or Laves phases formed at high Ti-concentrations do not directly impair the ability of the high-Ti CCAs to passivate. Additionally, both stochiometric dissolution rates obtained via AESEC (Figure 8) and non-preferential growth of pits following initiation (Figure 9) suggest neither phase is suggested to preferentially dissolve during polarization in 0.1 M NaCl pH 4, indicating protectiveness of the oxide layer

over both phases. One possible explanation relies on the composition of the phases. The strong corrosion resistance of Ti-6.0 has been previously tied to ensuring both phases are enriched in at least one passivating elements (e.g., Cr in the FCC matrix, Ti in the $L2_1$ second phase) [35, 40]. Given the prominence of Ti(IV) in the passive films (Figure 15, Table VIII) and that pure Ti is shown to be more resistant to localized breakdown than Al under the conditions used in this work [35], it may be reasonably inferred that the incremental contributions of increased Ti concentration on the $L2_1$ phase are less detrimental than those of increasing Al concentrations, leading to the improved corrosion resistance of high-Ti CCAs relative to high-Al CCAs. Similarly, the Laves phase introduced in Ti-9.6 and Ti-13.0 is enriched in Cr and Mo, two element capable of forming stable passive film. The formation of a Laves phase led to decreasing Cr concentration in other phases. For instance, the Cr concentration in the FCC matrix is lower in Ti-13.0 (10.2 at. %) than both the single-phase Ti-0 (10.9 at. %) and two-phase Ti-6.0 (11.1 at. %) (Table III). Regardless, passivity may be achieved by CCAs with Cr concentrations as low as 10 at. % in the presence of other passivators such as the ~7 at. % Ti present in the FCC phase of Ti-13.0 (Table II) [35], however; in addition to the ability to passivate, the effect of Ti on the breakdown behavior in Cl^- containing solutions must also be considered.

Ti-0 is suggested by both potentiodynamic polarization (Figures 5, 7, 10, Tables IV, V) and EIS of the air-formed oxide (Figure 11, Table VI) to have inferior corrosion resistance to the Ti-containing CCAs. following trends established for the Fe-Ti system in concentrated HCl by Kim et al. [34]. Such improvements indicate Ti addition is beneficial in a single phase microstructure for its contributions to passivity, and can even improve corrosion resistance despite the introduction of a new phase [53]. However, the introduction of a multi-phase microstructure can promote localized corrosion, as identified by the preferential pitting at phase interfaces observed in micrographs obtained following polarization (Figure 9). Low levels Ti addition improved the pitting resistance of Ti-0 across a range of Cl concentrations (Figure 7) despite the formation of an FCC-$L2_1$ interface, but such trends were not present at high Ti

concentrations. For instance, E_{pit} of Ti-9.6 and Ti-13.0 is lower than that of Ti-6.0 with passive films both during air exposure (Figure 10, Table V) and potentiodynamic polarization of a reduced surface (Figures 5, 6, Table IV). Similar trends were also observed with regards to repassivation (Figure 6, Tables IV, V). Given that pitting was disproportionately observed at or near phase interfaces for the multi-phase CCAs, the effect of microstructure and phase interfaces must be considered in future work.

Thus, trade-offs may be present between global beneficial effects of Ti concentration on passivity and adverse consequences of microstructurally influenced localized corrosion. E_{pit} was not suggested to decrease until Ti concentrations of 9.6 at. % (Figure 5, 6, 10, Table IV, V), the first CCA that had a three-phase microstructure (Figures 1, 3, Table II), possibly indicating such adverse microstructural effects are more prominent at the point of initiation of the Laves phase. However, the Laves interfaces do not show more frequent pitting than other interfaces (Figure 9). Thus, the effects of Laves presence on overall alloy must be considered. For instance, while the FCC phase of Ti-13.0 maintains sufficient Cr concentrations to form a stable passive film, it could possibly be more susceptible to localized corrosion.

Compositions maximizing Ti concentration while preserving a two-phase microstructure could be pursued for corrosion resistance; however, it would be necessary to ensure each phase maintains an adequate concentration of passivating elements. Furthermore, targeting such a two-phase microstructure might be restricted to specific phase structures such as FCC + $L2_1$. The Fe-Cr-Al-Ti system is a notable example, where increasing Ti concentration led to the formation of a Laves phase which, as in the case of the evaluated CCA system, was suggested to harm the corrosion resistance [43]. increasing Ti concentrations may also increase the likelihood of formation of Ti nitride impurities such as those observed in Figure 4. In addition to microstructural drawbacks, decreases in corrosion resistance at high Ti concentrations could be attributable to the lower Ti(IV) surface cation fractions and/or decreased concentrations at the oxide-metal interface (Figure 15, Table VIII). Regardless of mechanism, it is of note

that the optimal composition would be significantly dependent on the alloy system as well as on other processing parameters that may affect alloy microstructure.

5.0 Conclusions

Five CCAs in the Al-Cr-Fe-Mn-Mo-Ni-Ti system with variable Ti concentrations ranging from 0 to 13.0 at. % were synthesized, homogenized, and evaluated for corrosion resistance. The effects of Ti concentration on microstructure, passivity, localized corrosion, and passive film chemistry were evaluated. The following conclusions were observed:

- The microstructure transitioned from single-phase FCC, to an FCC matrix enriched in Fe, Cr, and Mo relative to bulk alloy compositions with $L2_1$ second phase regions enriched in Al, Cr, and Ti. At Ti concentrations above 9.6 at. %, a third phase of likely C14 Laves structure enriched in Fe, Cr, and Mo was present.
- Electrochemical parameters traditionally associated with passivity (e.g., i_{pass}, R_p) often showed improved results with increasing Ti concentrations whereas those associated with localized breakdown (e.g., E_{pit}, E_{rep}) were maximized at 6 at. % Ti before decreasing at higher Ti concentrations. High-Ti concentration may harm the resistance to localized corrosion by initiating second and third-phase formation of a complex morphology where the interfaces between these phases served as a preferential pitting site.
- The passive film is suggested to be dominated by Cr(III) and Ti(IV). Ti(IV) was a major passivator in Ti containing alloys. However, Ti(IV) surface cation fractions observed via XPS did not increase between the two CCAs evaluated, potentially due to differing passive film layering and/or changes in thicknesses.

Acknowledgments

This work was supported by the United States Office of Naval Research grants #N00014-23-1-2441 and #N00014-19-1-2420 under the directorship of David Shifler. AESEC equipment was funded under Agence Nationale de Recherche award # ANR-20-CE08-0031 (TAPAS 2020). The contributions of Jie Qi, Mark A. Wischhusen and Sean R. Agnew to CCA synthesis, processing, microstructural characterization, and prediction are acknowledged. SEM, XPS, and XRD facilities and training was provided by the University of Virginia Nanomaterials Characterization Facility. The PHI VersaProbe III was supported NSF award # 162601 with technical assistance provided by Catherine A. Dukes and Angela Y. Gerard.

References

[1] A. Chavan, S. Mandal, M. Roy, Cobalt free refractory high entropy alloys for total joint arthroplasty: In-vitro wear, corrosion and cytocompatibility evaluation, Journal of Alloys and Compounds, 938 (2023) 168499.
[2] B. Chen, X. Li, W. Chen, L. Shang, L. Jia, Microstructural evolution, mechanical and wear properties, and corrosion resistance of as-cast CrFeNbTiMox Refractory high entropy alloys, Intermetallics, 155 (2023) 107829.
[3] J. Jayaraj, C. Thinaharan, S. Ningshen, C. Mallika, U. Kamachi Mudali, Corrosion behavior and surface film characterization of TaNbHfZrTi high entropy alloy in aggressive nitric acid medium, Intermetallics, 89 (2017) 123-132.
[4] M. Li, Q. Chen, X. Cui, X. Peng, G. Huang, Evaluation of corrosion resistance of the single-phase light refractory high entropy alloy TiCrVNb0.5Al0.5 in chloride environment, Journal of Alloys and Compounds, 857 (2021) 158278.
[5] D.B. Miracle, O.N. Senkov, A critical review of high entropy alloys and related concepts, Acta Materialia, 122 (2017) 448-511.
[6] W. Xiong, L. Cheng, S. Zhan, A.X.Y. Guo, P.K. Liaw, S.C. Cao, Recent Advances on Lightweight High-Entropy Alloys: Process, Design, and Applications, High Entropy Alloys & Materials, (2023).
[7] G.-S. Ham, Y.-K. Kim, Y.S. Na, K.-A. Lee, Effect of Ti Addition on the Microstructure and High-Temperature Oxidation Property of AlCoCrFeNi High-Entropy Alloy, Metals and Materials International, 27 (2021) 156-165.
[8] U. Martin, J. Ress, P. Pérez, P. Adeva, D.M. Bastidas, Corrosion Behavior of Al10Cr30Fe25Mn30Ti5 High-Entropy Alloy: Microstructural, Electrochemical, and Surface Analysis, in: Metals, 2022.
[9] W. Qi, W. Wang, X. Yang, G. Zhang, W. Ye, Y. Su, Y. Li, S. Chen, Effects of Al and Ti co-doping on the strength-ductility- corrosion resistance of CoCrFeNi-AlTi high-entropy alloys, Journal of Alloys and Compounds, 925 (2022) 166751.
[10] X.X. Liu, S.G. Ma, W.D. Song, D. Zhao, Z.H. Wang, Microstructure evolution and mechanical response of Co-free Ni2CrFeAl0.3Tix high-entropy alloys, Journal of Alloys and Compounds, 931 (2023) 167523.
[11] M. Wu, R.C. Setiawan, D.Y. Li, Benefits of passive element Ti to the resistance of AlCrFeCoNi high-entropy alloy to corrosion and corrosive wear, Wear, 492-493 (2022) 204231.
[12] P. Chauhan, S. Yebaji, V.N. Nadakuduru, T. Shanmugasundaram, Development of a novel light weight Al35Cr14Mg6Ti35V10 high entropy alloy using mechanical alloying and spark plasma sintering, Journal of Alloys and Compounds, 820 (2020) 153367.
[13] R. Feng, C. Lee, M. Mathes, T.T. Zuo, S. Chen, J. Hawk, Y. Zhang, P. Liaw, Design of Light-Weight High-Entropy Alloys, Entropy, 18 (2016) 333.
[14] R. Feng, C. Zhang, M.C. Gao, Z. Pei, F. Zhang, Y. Chen, D. Ma, K. An, J.D. Poplawsky, L. Ouyang, Y. Ren, J.A. Hawk, M. Widom, P.K. Liaw, High-throughput design of high-performance lightweight high-entropy alloys, Nature Communications, 12 (2021) 4329.
[15] X. Huang, J. Miao, A.A. Luo, Lightweight AlCrTiV high-entropy alloys with dual-phase microstructure via microalloying, Journal of Materials Science, 54 (2019) 2271-2277.
[16] Z.-S. Nong, Y.-N. Lei, J.-C. Zhu, Wear and oxidation resistances of AlCrFeNiTi-based high entropy alloys, Intermetallics, 101 (2018) 144-151.
[17] E. Osei-Agyemang, G. Balasubramanian, Surface oxidation mechanism of a refractory high-entropy alloy, npj Materials Degradation, 3 (2019) 20.
[18] Y. Qiu, S. Thomas, M.A. Gibson, H.L. Fraser, N. Birbilis, Corrosion of high entropy alloys, npj Materials Degradation, 1 (2017) 15.

[19] J.D. Jackson, W.K. Boyd, Corrosion of Titanium, Defense Metals Information Center, Battelle Memorial Institute, 1966.
[20] J.J. Noël, N. Ebrahimi, D.W. Shoesmith, Corrosion of Titanium and Titanium Alloys, in, 2018.
[21] N.P. Sazhin, U.S.N. Aeronautics, S. Administration, Titanium Alloys for Modern Technology, National Aeronautics and Space Administration, for sale by the Clearinghouse for Federal Scientific and Technical Information, Springfield, Va., 1959.
[22] V.A. Alves, R.Q. Reis, I.C.B. Santos, D.G. Souza, T. de F. Gonçalves, M.A. Pereira-da-Silva, A. Rossi, L.A. da Silva, In situ impedance spectroscopy study of the electrochemical corrosion of Ti and Ti–6Al–4V in simulated body fluid at 25°C and 37°C, Corrosion Science, 51 (2009) 2473-2482.
[23] M.A. Khan, R.L. Williams, D.F. Williams, The corrosion behaviour of Ti–6Al–4V, Ti–6Al–7Nb and Ti–13Nb–13Zr in protein solutions, Biomaterials, 20 (1999) 631-637.
[24] S. Tamilselvi, V. Raman, N. Rajendran, Corrosion behaviour of Ti–6Al–7Nb and Ti–6Al–4V ELI alloys in the simulated body fluid solution by electrochemical impedance spectroscopy, Electrochimica Acta, 52 (2006) 839-846.
[25] M. Atapour, A. Pilchak, G.S. Frankel, J.C. Williams, M.H. Fathi, M. Shamanian, Corrosion Behavior of Ti-6Al-4V with Different Thermomechanical Treatments and Microstructures, Corrosion, 66 (2010) 065004-065004-065009.
[26] J. Yang, H. Yang, H. Yu, Z. Wang, X. Zeng, Corrosion Behavior of Additive Manufactured Ti-6Al-4V Alloy in NaCl Solution, Metallurgical and Materials Transactions A, 48 (2017) 3583-3593.
[27] J.J. Noel, The electrochemistry of titanium corrosion, (1999).
[28] M. Pourbaix, Atlas of electrochemical equilibria in aqueous solutions, in, National Association of Corrosion Engineers, Houston, Tex., 1974.
[29] C.K. Dyer, J.S.L. Leach, Breakdown and Efficiency of Anodic Oxide Growth on Titanium, Journal of The Electrochemical Society, 125 (1978) 1032.
[30] J.S.L. Leach, B.R. Pearson, Crystallization in anodic oxide films, Corrosion Science, 28 (1988) 43-56.
[31] M.R. Kozlowski, P.S. Tyler, W.H. Smyrl, R.T. Atanasoski, Anodic TiO2 Thin Films: Photoelectrochemical, Electrochemical, and Structural Study of Heat-Treated and Modified Films, Journal of The Electrochemical Society, 136 (1989) 442.
[32] P.S. Tyler, M.R. Kozlowski, W.H. Smyrl, R.T. Atanasoski, Photoelectrochemical microscopy as a probe of localized properties of thin TiO2 films, Journal of Electroanalytical Chemistry, 237 (1987) 295-302.
[33] O. Durante, C. Di Giorgio, V. Granata, J. Neilson, R. Fittipaldi, A. Vecchione, G. Carapella, F. Chiadini, R. DeSalvo, F. Dinelli, V. Fiumara, V. Pierro, I.M. Pinto, M. Principe, F. Bobba, Emergence and Evolution of Crystallization in TiO2 Thin Films: A Structural and Morphological Study, in: Nanomaterials, 2021.
[34] H. Kim, N. Akao, N. Hara, K. Sugimoto, Comparison of Corrosion Resistances Between Fe2 O 3 - TiO2 Artificial Passivation Film and Passivation Film on Fe-Ti Alloy, Journal of The Electrochemical Society, 145 (1998) 2818.
[35] S.B. Inman, D. Sur, J. Han, K. Ogle, J.R. Scully, Corrosion Behavior of a Compositionally Complex Alloy Utilizing Simultaneous Al, Cr, and Ti Passivation, Corroison Science, 217 (2023) 111138.
[36] W.-C. Luu, W.-C. Chiang, J.-K. Wu, Effect of Cr and Ti additions on the corrosion behavior of Fe3Al alloys in chloride-containing sulfuric acid solutions, Materials Letters, 59 (2005) 3295-3298.
[37] R.A. Rodríguez-Díaz, J. Uruchurtu-Chavarín, A. Molina-Ocampo, J. Porcayo-Calderón, M. González-Pérez, J.M. López-Oglesby, J.G. Gonzalez-Rodríguez, J.A. Juárez-Islas, Corrosion Behavior of Fe-Al Alloy Modified with Cr and Ti in Simulated Physiological Human Media, International Journal of Electrochemical Science, 8 (2013) 958-972.
[38] L. Kaufman, Calculation of multicomponent ceramic phase diagrams, Physica B+C, 150 (1988) 99-114.

[39] A.S. Berezhnoi, N.V. Gul´ko, Phase Diagrams of the Systems Cr2O3-TiO2 and Cr2O3-ZrO2 (in Ukrainian), Dopovidi An Ukrainskoi RSR, serija B, Geologija, Geofisika, Khimija i Biologija, 1968 (1968) 250-253.
[40] S.B. Inman, J.R. Scully, Design and Discovery of Compositionally Complex Alloys (CCA) that Include High Corrosion Resistance, Corrosion, 80 (2024) 250-258.
[41] J.R. Scully, S.B. Inman, A.Y. Gerard, C.D. Taylor, W. Windl, D.K. Schreiber, P. Lu, J.E. Saal, G.S. Frankel, Controlling the corrosion resistance of multi-principal element alloys, Scripta Materialia, 188 (2020) 96-101.
[42] Y. Qiu, R. Liu, T. Gengenbach, O. Gharbi, S. Choudhary, S. Thomas, H.L. Fraser, N. Birbilis, Real-time dissolution of a compositionally complex alloy using inline ICP and correlation with XPS, npj Materials Degradation, 4 (2020) 7.
[43] D. Sur, S.B. Inman, K.L. Anderson, J. Qi, M. Barbiari, J.R. Scully, Passivation behavior of Fe-Cr-Al-Ti alloys in sulfate containing aqueous environments, In Progress.
[44] M. Ibrahim, S. El-Hadad, W. Khalifa, M. Shoeib, Effect of Ti Addition and Heat Treatment on Electrochemical Properties of Cast Fe35Mn31Ni18Al13Tix HEAs, International Journal of Metalcasting, 17 (2023) 888-899.
[45] X. Liang, Y. Su, T. Yang, Z. Dai, Y. Wang, Effect of Ti Addition on the Microstructure and Corrosion Resistance of AlCrCuFeNiNb0.2 High-Entropy Alloy, JOM, 75 (2023) 428-436.
[46] M.C. Groenenboom, R.M. Anderson, D.J. Horton, Y. Basdogan, D.F. Roeper, S.A. Policastro, J.A. Keith, Doped Amorphous Ti Oxides To Deoptimize Oxygen Reduction Reaction Catalysis, The Journal of Physical Chemistry C, 121 (2017) 16825-16830.
[47] S. Li, J. Fu, Improvement in corrosion protection properties of TiO2 coatings by chromium doping, Corrosion Science, 68 (2013) 101-110.
[48] A. Chen, W.-F. Chen, T. Majidi, B. Pudadera, A. Atanacio, M. Manohar, L.R. Sheppard, R. Liu, C.C. Sorrell, P. Koshy, Mo-doped, Cr-Doped, and Mo–Cr codoped TiO2 thin-film photocatalysts by comparative sol-gel spin coating and ion implantation, International Journal of Hydrogen Energy, 46 (2021) 12961-12980.
[49] S. Ishihara, E. Tochigi, R. Ishikawa, N. Shibata, Y. Ikuhara, Atomic structures of Ti-doped α-Al2O3 Σ13 grain boundary with a small amount of Si impurity, Journal of the American Ceramic Society, 103 (2020) 6659-6665.
[50] C. Ma, K. Chen, C. Liang, C.-W. Nan, R. Ishikawa, K. More, M. Chi, Atomic-scale origin of the large grain-boundary resistance in perovskite Li-ion-conducting solid electrolytes, Energy & Environmental Science, 7 (2014) 1638-1642.
[51] Y. Qiu, S. Thomas, R.K. Gupta, T. Gengenbach, R. Jones, N. Birbilis, A Surface Study of the Native Oxide upon a Compositionally Complex Alloy, Corrosion, 74 (2018) 1312-1317.
[52] D.D. Macdonald, The Point Defect Model for the Passive State, Journal of The Electrochemical Society, 139 (1992) 3434.
[53] Y. Qiu, M.A. Gibson, H.L. Fraser, N. Birbilis, Corrosion characteristics of high entropy alloys, Materials Science and Technology, 31 (2015) 1235-1243.
[54] D.H. Xiao, P.F. Zhou, W.Q. Wu, H.Y. Diao, M.C. Gao, M. Song, P.K. Liaw, Microstructure, mechanical and corrosion behaviors of AlCoCuFeNi-(Cr,Ti) high entropy alloys, Materials & Design, 116 (2017) 438-447.
[55] B. Ren, R. Zhao, Z.-X. Liu, S.-k. Guan, H.-S. Zhang, Microstructure and properties of Al0.3CrFe1.5MnNi0.5Ti x and Al0.3CrFe1.5MnNi0.5Si x high-entropy alloys, Rare Metals, 33 (2014) 149-154.
[56] X.W. Qiu, Y.P. Zhang, C.G. Liu, Effect of Ti content on structure and properties of Al2CrFeNiCoCuTix high-entropy alloy coatings, Journal of Alloys and Compounds, 585 (2014) 282-286.

[57] Y.J. Zhou, Y. Zhang, Y.L. Wang, G.L. Chen, Solid solution alloys of AlCoCrFeNiTix with excellent room-temperature mechanical properties, Applied Physics Letters, 90 (2007) 181904.
[58] K. Ishikawa, I. Ohnuma, R. Kainuma, K. Aoki, K. Ishida, Phase equilibria and stability of Heusler-type aluminides in the NiAl–Ni2AlTi–Ni2AlY (Y: V, Cr or Mn) systems, Journal of Alloys and Compounds, 367 (2004) 2-9.
[59] Y. Xu, G. Wang, Q. Song, X. Lu, Z. Li, Q. Zhao, Y. Chen, Microstructure, mechanical properties, and corrosion resistance of SiC reinforced AlxCoCrFeNiTi1-x high-entropy alloy coatings prepared by laser cladding, Surface and Coatings Technology, 437 (2022) 128349.
[60] M.M. Garlapati, M. Vaidya, A. Karati, S. Mishra, R. Bhattacharya, B.S. Murty, Influence of Al content on thermal stability of nanocrystalline AlxCoCrFeNi high entropy alloys at low and intermediate temperatures, Advanced Powder Technology, 31 (2020) 1985-1993.
[61] F. Liu, Q. Song, R. Chen, W. Li, X. Song, J. Sun, C. Wang, Effects of Al and Co contents on the microstructure and properties of AlxCoCryFeNi high-entropy alloys, Materials Characterization, 203 (2023) 113108.
[62] Y. Shi, L. Collins, R. Feng, C. Zhang, N. Balke, P.K. Liaw, B. Yang, Homogenization of AlxCoCrFeNi high-entropy alloys with improved corrosion resistance, Corrosion Science, 133 (2018) 120-131.
[63] D. Yang, Y. Liu, H. Jiang, M. Liao, N. Qu, T. Han, Z. Lai, J. Zhu, A novel FeCrNiAlTi-based high entropy alloy strengthened by refined grains, Journal of Alloys and Compounds, 823 (2020) 153729.
[64] C.-C. Yen, H.-N. Lu, M.-H. Tsai, B.-W. Wu, Y.-C. Lo, C.-C. Wang, S.-Y. Chang, S.-K. Yen, Corrosion mechanism of annealed equiatomic AlCoCrFeNi tri-phase high-entropy alloy in 0.5 M H2SO4 aerated aqueous solution, Corrosion Science, 157 (2019) 462-471.
[65] Q. Zhao, Z. Pan, X. Wang, H. Luo, Y. Liu, X. Li, Corrosion and passive behavior of AlxCrFeNi3−x (x = 0.6, 0.8, 1.0) eutectic high entropy alloys in chloride environment, Corrosion Science, 208 (2022) 110666.
[66] J. Joseph, M. Annasamy, S.R. Kada, P.D. Hodgson, M.R. Barnett, D.M. Fabijanic, Optimising the Al and Ti compositional window for the design of γ' (L12)-strengthened Al–Co–Cr–Fe–Ni–Ti high entropy alloys, Materials Science and Engineering: A, 835 (2022) 142620.
[67] S.B. Inman, M.A. Wischhusen, J. Qi, J. Poon, S.R. Agnew, J.R. Scully, Variation of the Passive Film on Compositionally Concentrated Dual-phase Al0.3Cr0.5Fe2Mn0.25Mo0.15Ni1.5Ti0.3 and Implications for Corrosion, Submitted to Metallurgical and Materials Transactions A, (2024).
[68] J.J. Bhattacharyya, S.B. Inman, M.A. Wischhusen, J. Qi, J. Poon, J.R. Scully, S.R. Agnew, Light Weight, Low Cost, and Compositionally Complex Multiphase Alloys with Optimized Strength, Ductility and Corrosion Resistance: Discovery, Design and Mechanistic Understandings, Materials & Design, 228 (2023).
[69] S.B. Inman, J. Han, A.Y. Gerard, J. Qi, M.A. Wischhusen, S.R. Agnew, S.J. Poon, K. Ogle, J.R. Scully, Effect of Mn Content on the Passivation and Corrosion of Al0.3Cr0.5Fe2MnxMo0.15Ni1.5Ti0.3 Compositionally Complex Face-Centered Cubic Alloys, Corrosion, 78 (2021) 32-48.
[70] S.B. Inman, J. Han, M.A. Wischhusen, J. Qi, S.R. Agnew, K. Ogle, J.R. Scully, Passivation and Localized Corrosion Resistance of Al0.3Cr0.5Fe2MoxNi1.5Ti0.3 Compositionally Complex Alloys: Effect of Mo Content, Corroison Science, 227 (2024) 111692.
[71] Y.-M. Chen, N.G. Rudawski, E. Lambers, M.E. Orazem, Application of impedance spectroscopy and surface analysis to obtain oxide film thickness, Journal of The Electrochemical Society, 164 (2017) C563.
[72] B. Hirschorn, M.E. Orazem, B. Tribollet, V. Vivier, I. Frateur, M. Musiani, Determination of effective capacitance and film thickness from constant-phase-element parameters, Electrochimica Acta, 55 (2010) 6218-6227.
[73] K. Lutton, K. Gusieva, N. Ott, N. Birbilis, J.R. Scully, Understanding multi-element alloy passivation in acidic solutions using operando methods, Electrochemistry Communications, 80 (2017) 44-47.

[74] K. Ogle, Atomic Emission Spectroelectrochemistry: Real-Time Rate Measurements of Dissolution, Corrosion, and Passivation, Corrosion, 75 (2019) 1398-1419.
[75] J. Baltrusaitis, B. Mendoza-Sanchez, V. Fernandez, R. Veenstra, N. Dukstiene, A. Roberts, N. Fairley, Generalized molybdenum oxide surface chemical state XPS determination via informed amorphous sample model, Applied Surface Science, 326 (2015) 151-161.
[76] M.C. Biesinger, L.W.M. Lau, A.R. Gerson, R.S.C. Smart, Resolving surface chemical states in XPS analysis of first row transition metals, oxides and hydroxides: Sc, Ti, V, Cu and Zn, Applied Surface Science, 257 (2010) 887-898.
[77] M.C. Biesinger, B.P. Payne, A.P. Grosvenor, L.W.M. Lau, A.R. Gerson, R.S.C. Smart, Resolving surface chemical states in XPS analysis of first row transition metals, oxides and hydroxides: Cr, Mn, Fe, Co and Ni, Applied Surface Science, 257 (2011) 2717-2730.
[78] A. Obrosov, R. Gulyaev, A. Zak, M. Ratzke, M. Naveed, W. Dudzinski, S. Weiß, Chemical and Morphological Characterization of Magnetron Sputtered at Different Bias Voltages Cr-Al-C Coatings, in: Materials, 2017.
[79] X. Yang, Y. Zhang, Prediction of high-entropy stabilized solid-solution in multi-component alloys, Materials Chemistry and Physics, 132 (2012) 233-238.
[80] D.J.M. King, S.C. Middleburgh, A.G. McGregor, M.B. Cortie, Predicting the formation and stability of single phase high-entropy alloys, Acta Materialia, 104 (2016) 172-179.
[81] J.D. Henderson, X. Li, D.W. Shoesmith, J.J. Noël, K. Ogle, Molybdenum surface enrichment and release during transpassive dissolution of Ni-based alloys, Corrosion Science, 147 (2019) 32-40.
[82] J. Han, X. Li, A.Y. Gerard, P. Lu, J.E. Saal, G.S. Frankel, K. Ogle, J.R. Scully, Potential Dependent Mn Oxidation and Its Role in Passivation of Ni38Fe20Cr22Mn10Co10 Multi-Principal Element Alloy Using Multi-Element Resolved Atomic Emission Spectroelectrochemistry, Journal of The Electrochemical Society, 168 (2021) 051508.
[83] J.R. Scully, D.C. Silverman, M.W. Kendig, Electrochemical Impedance: Analysis and Interpretation, in, 1993.
[84] J.D. Cox, D.D. Wagman, V.A. Medvedev, CODATA Key Values for Thermodynamics, in, New York, 1989.
[85] S.E. Ziemniak, L.M. Anovitz, R.A. Castelli, W.D. Porter, Thermodynamics of Cr2O3, FeCr2O4, ZnCr2O4, and CoCr2O4, The Journal of Chemical Thermodynamics, 39 (2007) 1474-1492.
[86] K. Orson, E. Romanovskaia, A. Costine, J. Han, K. Ogle, J.R. Scully, P. Reinke, Corrosion Resistance, Composition, and Stratification of Passive Films: Ni-22Cr and Ni-22Cr-6Mo Alloys Passivated and Exposure Aged in Acidic Chloride Solutions, Journal of The Electrochemical Society, 171 (2024) 011505.
[87] J.E. Saal, S. Kirklin, M. Aykol, B. Meredig, C. Wolverton, Materials Design and Discovery with High-Throughput Density Functional Theory: The Open Quantum Materials Database (OQMD), JOM, 65 (2013) 1501-1509.
[88] S. Kirklin, J.E. Saal, B. Meredig, A. Thompson, J.W. Doak, M. Aykol, S. Rühl, C. Wolverton, The Open Quantum Materials Database (OQMD): assessing the accuracy of DFT formation energies, npj Computational Materials, 1 (2015) 15010.
[89] K. Wang, J. Han, A.Y. Gerard, J.R. Scully, B.-C. Zhou, Potential-pH diagrams considering complex oxide solution phases for understanding aqueous corrosion of multi-principal element alloys, npj Materials Degradation, 4 (2020) 35.
[90] H.D. Werner, N. Jahrbuch Miner. Monatshefte, (1974) 218-234.
[91] S.M. Lang, C.L. Fillmore, L.H. Maxwell, The System Beryllia-Alumina-Titania: Phase Relations and General Physical Properties of ThreeComponent Porcelains, Journal of Research of the National Bureau of Standards 48 (1952) 298-312.

Figure 1: XRD patterns of synthesized CCAs following 6-hour homogenization at 1070˚C with indexed peaks for the FCC, $L2_1$, phases with additional peaks characteristic of the suggested Laves phase are identified.

Figure 2: Isopleth diagram of $Al_{0.3}Cr_{0.5}Fe_2Mn_{0.25}Mo_{0.15}Ni_{1.5}Ti_x$ system produced in ThermoCalc with TCHEA3 database. Regions consisting of the CCA series following homogenization are labeled with predicted microstructure. The temperature for heat treatment is identified by the dashed line with synthesized compositions indicated by black circles.

Figure 3: BSE micrographs of CCAs following 6-hour homogenization at 1070˚C.

Figure 4: EDS mapping of a) Ti-6.0 (FCC + $L2_1$) and b) Ti-9.6 (FCC + $L2_1$ + Laves) microstructures.

Figure 5: a) E-log(i) and b) -Z" plots obtained during polarization of CCAs in 0.01 M NaCl (pH ~5.75) following cathodic pre-treatment (-1.3 V_{SCE}, 600 s). Dashed lines indicate stability ranges for the pure stoicometric oxides of passive species formed on their pure constituent elements and water constituents at a pH of 5.75 predicted by Hydra Medusa software. Cyclic polarization scans including the downward direction are included in the supplementary information section.

Figure 6: Summary of potentiodynamic polarization corrosion parameters shown in Table IV as a function of Ti concentration and microstructure. Error bars for each parameter indicate a one standard deviation range.

Figure 7: E-log(i) plots obtained during polarization of a) Ti-0 and b) Ti-6.0 in NaCl ranging in concentrations from 0.001 to 1.0 M (pH ~5.5-6.0) following cathodic pre-treatment (-1.3 V_{SCE}, 600 s) along with c) comparisons of pitting potential for each CCA and 316L as a function of electrolyte concentration. Error bars for each parameter indicate a one standard deviation range. Cyclic polarization scans including the downward direction are included in the supplementary information section.

Figure 8: Normalized equivalent current densities obtained from AESEC during potentiodynamic polarization of Ti-6.0 in 0.1 M NaCl adjusted to pH 4. Al equivalent dissolution current densities are not shown due to high levels of noise, but are below the detection limits in the transpassive region.

Figure 9: BSE of micrographs showing pit locations and morphology relative to CCA microstructural features. Potentiodynamic polarization in 0.01 M NaCl described above was terminated upon reaching a current density of 10^{-5} A/cm^2 prior to imaging. Pit locations illustrating transition from random to interface pitting are circled.

Figure 10: a) E-log(i) and b) -Z" plots obtained during polarization of CCAs with air-formed oxide in 0.01 M NaCl (pH ~5.75). Dashed lines indicate stability ranges for the oxides of passive species formed on their pure constituent elements and water constituents at a pH of 5.75 predicted by Hydra Medusa

software. Cyclic polarization scans including the downward direction are included in the supplementary information section.

Figure 11: Bode plot obtained during EIS of CCAs with solution-exposed air-formed oxides at each CCAs OCP. Lines indicate best fits to a Randles circuit with parameters shown in Table VI.

Figure 12: a) Current density and b) in-situ -Z" measurements during potentiostatic film growth of CCAs at -0.25 V_{SCE} in 0.01 M NaCl (pH ~5.75) with a 6 s period following cathodic pre-treatment (-1.3 V_{SCE}, 600 s).

Figure 13: Bode plot obtained during EIS of CCAs with following potentiostatic oxide growth (40 ks, -0.25 V_{SCE}). Lines indicate best fits to a Randles circuit with parameters shown in Table VI.

Figure 14: Fit high-resolution spectra for selected CCAs following potentiostatic oxide growth (-0.25 V_{SCE}, 40 ks) in 0.01 M NaCl (pH ~5.75)

Figure 15: Surface cation fractions for selected CCAs from Table VII

Figure 16: Psudo-Convex Hull diagram containing formation energies for a range of oxide (moving from oxygen-sparce to oxygen-rich from left to right), hydroxide, and oxyhydroxide species possible for each constituent element obtained from Open Quantum Materials Database [88, 89]. Dashed lines indicate connections skipping over a chemical species for which thermodynamic data was not available.

Figure 1

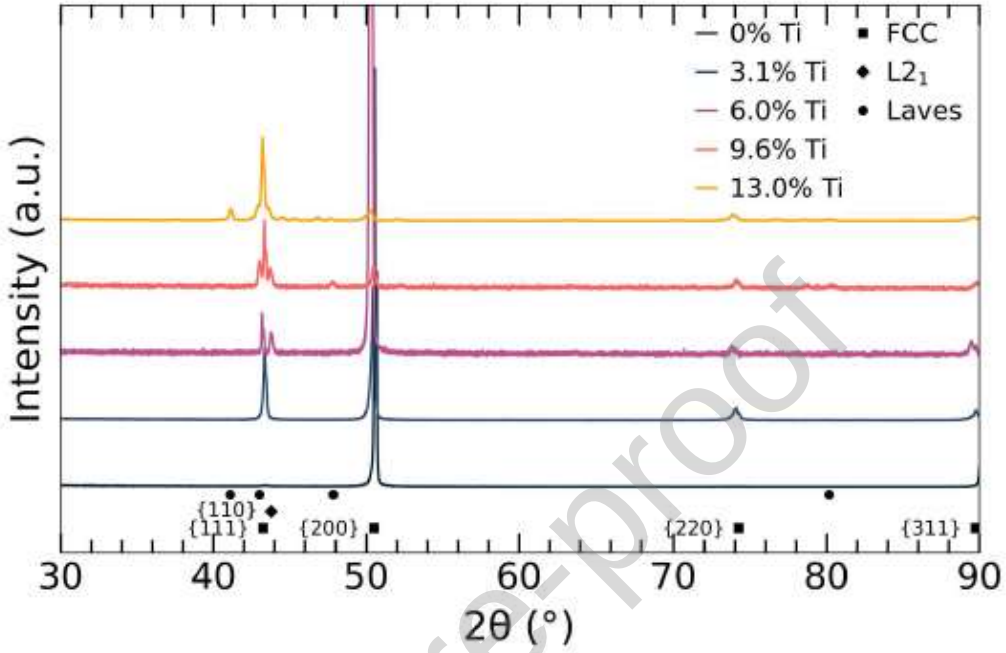

Figure 2

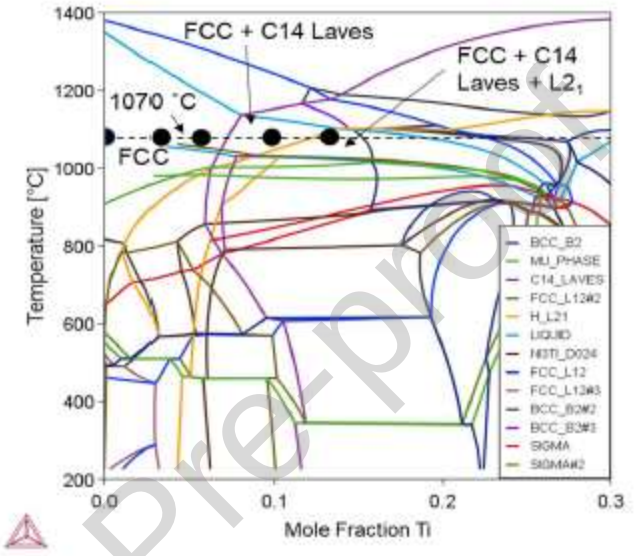

Figure 3

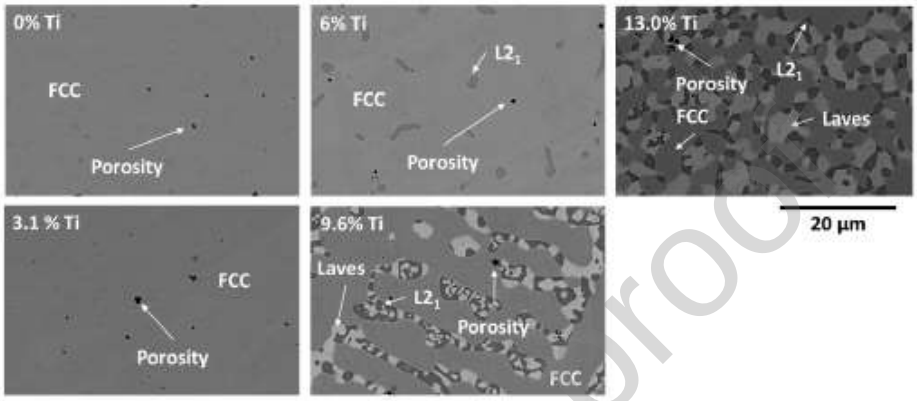

Figure 4

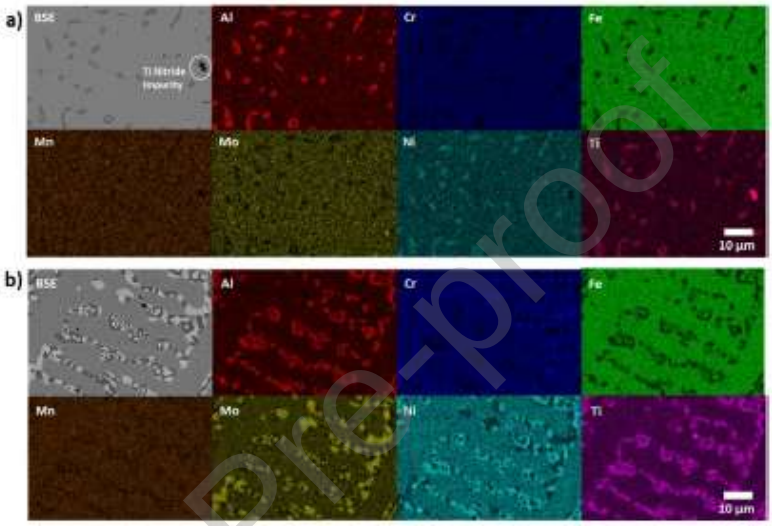

Figure 5

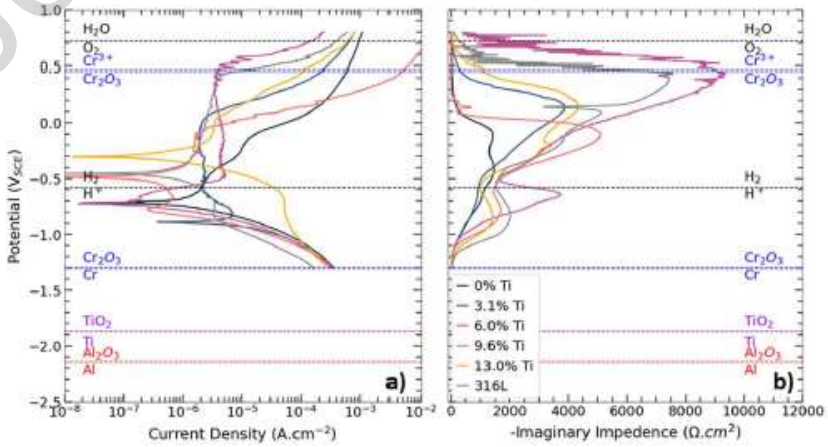

Figure 6

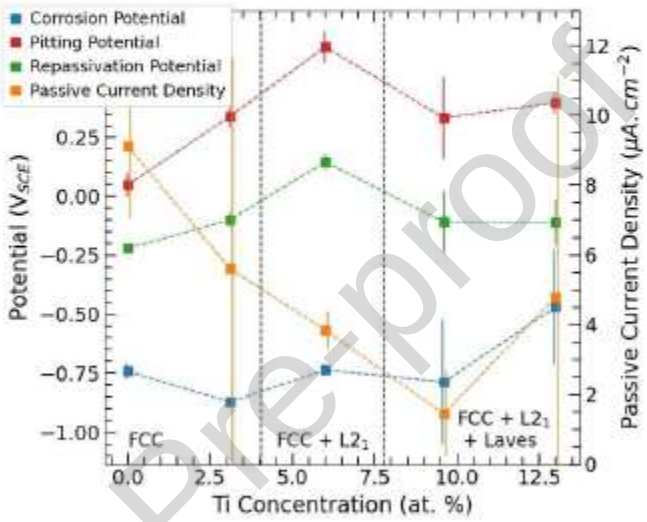

Figure 7

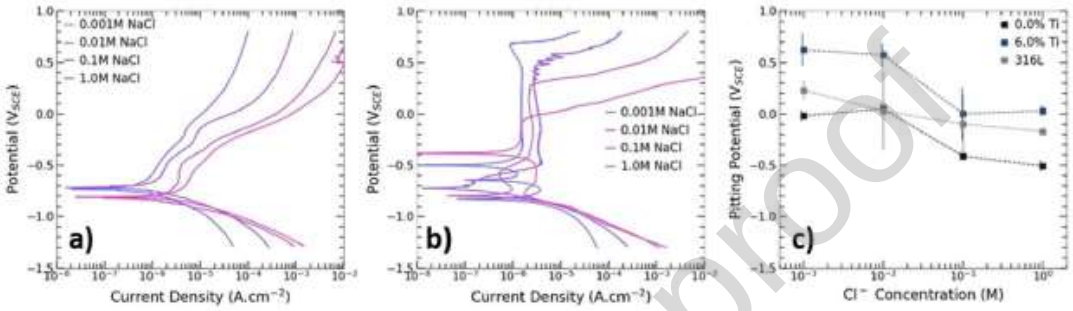

Figure 8

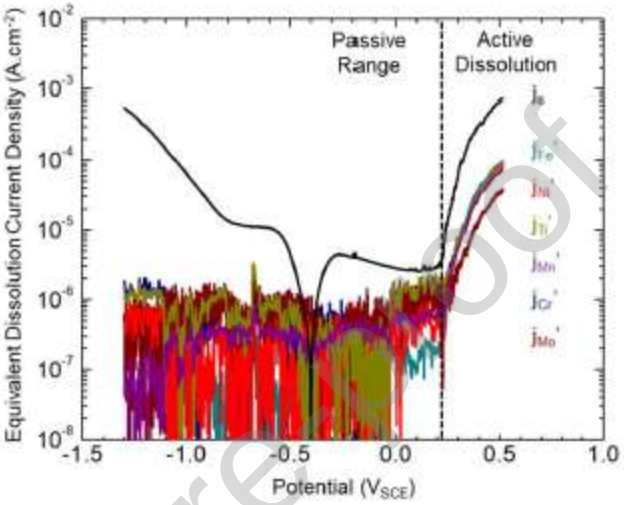

Figure 9

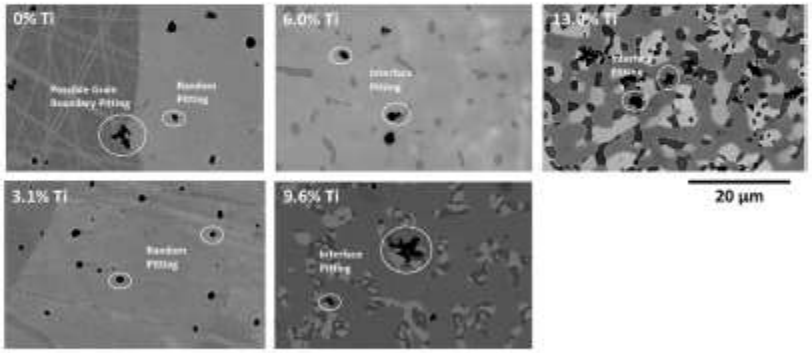

Figure 10

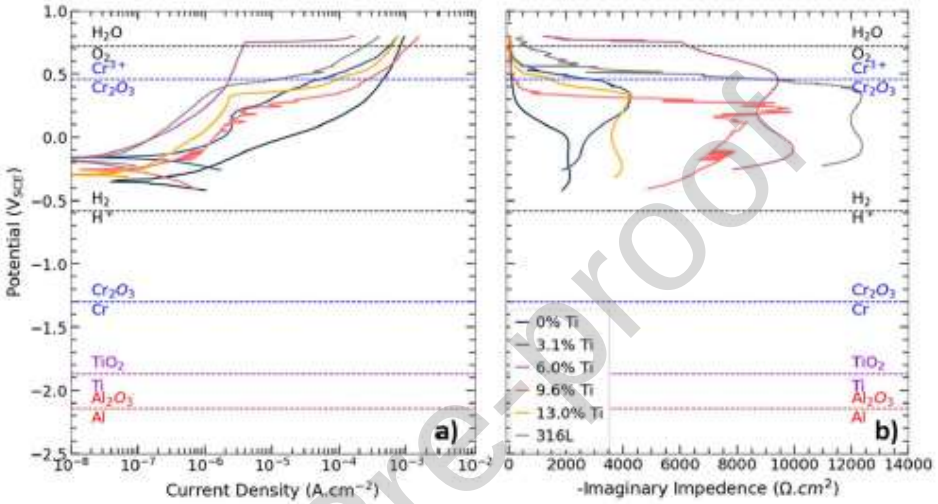

Figure 11

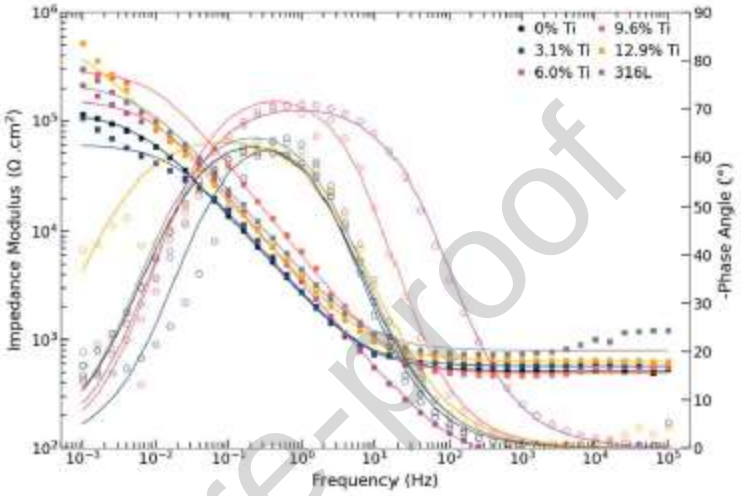

Figure 12

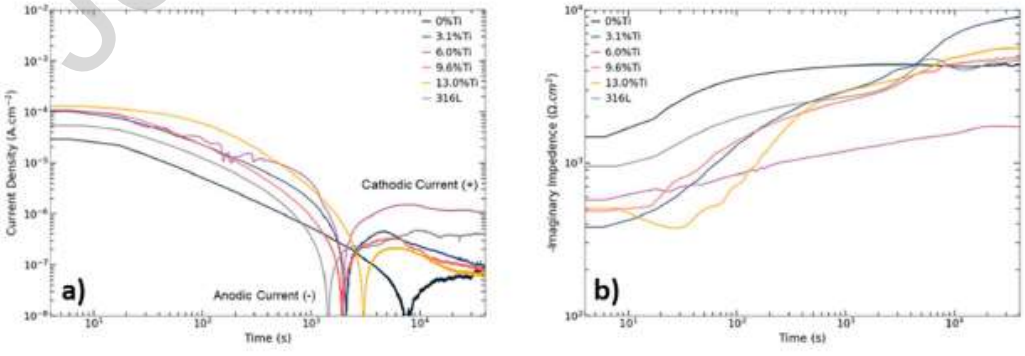

Figure 13

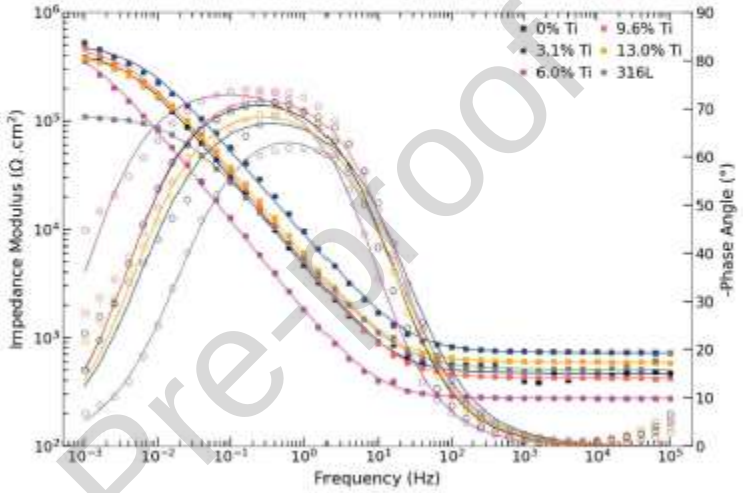

Figure 14

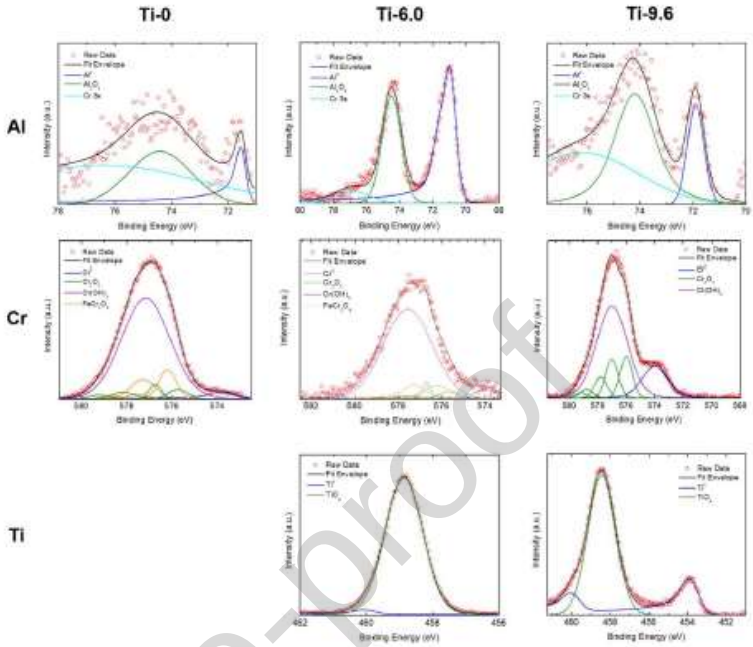

Figure 15

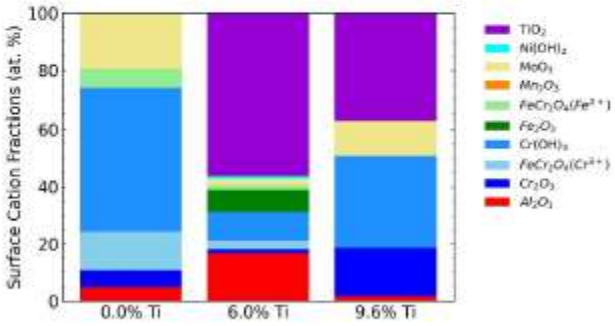

Figure 16

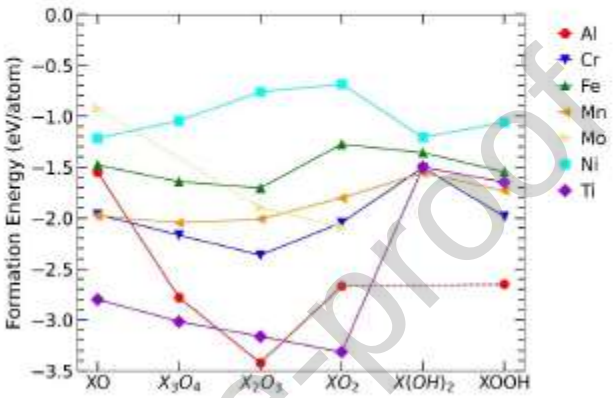

AuthorStatement

Samuel B. Inman: Conceptualization, Formal analysis, Investigation, Writing - Original Draft, Visualization. **Junsoo Han:** Investigation, Writing - Review & Editing. **Diego Ibarra Hoyos:** Investigation, Writing - Review & Editing. **S. Joseph Poon:** Writing - Review & Editing, Supervision, Funding acquisition. **Kevin M. Ogle:** Methodology, Supervision, Funding acquisition. **John R. Scully:** Conceptualization, Methodology, Writing - Review & Editing, Supervision, Project administration, Funding acquisition.

Table I: CCA compositions in atomic percent. Pure elements were massed to compositions below within 1% error prior to arc melting.

	Al	**Cr**	**Fe**	**Mn**	**Mo**	**Ni**	**Ti**
Ti-0	6.4	10.6	42.6	5.3	3.2	31.9	0.0
Ti-3.1	6.2	10.3	41.2	5.2	3.1	30.9	3.1
Ti-6.0	6.0	10.0	40.0	5.0	3.0	30.0	6.0
Ti-9.6	5.8	9.6	38.5	4.8	2.9	28.8	9.6

Ti-13.0	5.6	9.3	37.0	4.6	2.8	27.8	13.0

Table II: Phases present in CCAs following 6-hour homogenization at 1070 ˚C compared to computational predictions from CALPHAD shown in Figure 2.

Alloy	**Predicted Microstructure from Isopleth**	**Observed Microstructure**
Ti-0	FCC	FCC
Ti-3.1	FCC	FCC
Ti-6.0	FCC	FCC + $L2_1$
Ti-9.6	FCC + Laves	FCC + $L2_1$ + Laves
Ti-13.0	FCC + $L2_1$ + Laves	FCC + $L2_1$ + Laves

Table III: Phase compositions for selected alloys identified with EDS point scans. Each entry represents the mean value of at least three scans, while global compositions were obtained from quantitative analysis of the mapping area. Area fractions for each phase are identified by ImageJ threshold analysis.

Phase	**Al**	**Cr**	**Fe**	**Mn**	**Mo**	**Ni**	**Ti**	**Area Fraction**
$Al_{0.3}Cr_{0.5}Fe_2Mn_0Mo_{0.15}Ni_{1.5}$ (Ti-0)								
Matrix (FCC- Overall)	6.2	10.9	42.5	5.2	3.5	31.6	0.0	100 %
$Al_{0.3}Cr_{0.5}Fe_2Mn_{0.25}Mo_{0.15}Ni_{1.5}Ti_{0.3}$ (Ti-6.0)								
Matrix (FCC)	3.70	11.0	42.5	5.2	3.1	28.8	5.6	95.67 %
2nd Phase ($L2_1$)	14.3	3.5	17.1	4.2	0.9	44.1	15.8	4.33 %
Overall Composition	6.4	10.2	39.7	5.2	2.6	29.7	6.1	-
$Al_{0.3}Cr_{0.5}Fe_2Mn_{0.25}Mo_{0.15}Ni_{1.5}Ti_{0.7}$ (Ti-13.0)								
Matrix	3.8	10.2	42.7	5.0	2.2	28.6	7.6	67.14 %
2nd Phase ($L2_1$)	18.1	1.9	12.4	2.9	0.3	44.3	20.2	14.34%
3rd Phase (Laves)	2.0	15.3	44.7	4.3	7.8	15.6	10.3	18.52%
Overall Composition	5.7	9.8	38.3	4.6	2.8	29.0	9.8	-

Table IV: Key corrosion parameters obtained during potentiodynamic polarization of CCAs in 0.01 M NaCl (pH ~5.75) following cathodic pre-treatment (-1.3 V_{SCE}, 600 s). Each entry indicates the mean value with a one standard deviation bound.

Alloy	**Corrosion Potential (V_{SCE})**	**Pitting Potential (V_{SCE})**	**Repassivation Potential (V_{SCE})**	**Passive Current Density ($\mu A/cm^2$)**
Ti-0	-0.741 +/- 0.034	0.048 +/- 0.050	-0.220 +/- 0.014	9.1 +/- 2.1
Ti-3.1	-0.873 +/- 0.017	0.338 +/- 0.048	-0.100 +/- 0.035	5.6 +/- 6.1
Ti-6.0	-0.736 +/- 0.023	0.633 +/- 0.066	0.146 +/- 0.035	3.9 +/- 0.5
Ti-9.6	-0.787 +/- 0.262	0.332 +/- 0.173	-0.109 +/- 0.132	1.5 +/- 1.2
Ti-13.0	-0.469 +/- 0.244	0.397 +/- 0.045	-0.111 +/- 0.097	4.8 +/- 6.3
316L	-0.447 +/- 0.003	0.596 +/- 0.045	0.014 +/- 0.019	1.4 +/- 0.3

Table V: Key corrosion parameters obtained during potentiodynamic polarization of CCAs in 0.01 M NaCl (pH ~5.75) following 30 minute solution exposure of the air-formed oxide. Each entry indicates the mean value with a one standard deviation bound.

Alloy	**Corrosion Potential (V_{SCE})**	**Pitting Potential (V_{SCE})**	**Repassivation Potential (V_{SCE})**
Ti-0	-0.381 +/- 0.287	-0.092 +/- 0.319	-0.306 +/- -0.244
Ti-3.1	-0.219 +/- 0.062	0.251 +/- 0.103	-0.149 +/- 0.095
Ti-6.0	-0.173 +/- 0.008	0.631 +/- 0.243	0.185 +/- 0.152
Ti-9.6	-0.339 +/- 0.118	0.235 +/- 0.021	-0.253 +/- 0.004
Ti-13.0	-0.252 +/- 0.058	0.405 +/- 0.083	-0.090 +/- 0.064
316L	-0.182 +/- 0.016	0.437 +/- 0.025	0.004 +/- 0.058

Table VI: Randles circuit fit parameters for the EIS spectra of the air formed oxides exposed to solution at OCP.

Alloy	**Ti-0**	**Ti-3.1**	**Ti-6.0**	**Ti-9.6**	**Ti-13.0**	**316L**
R_p (kohm.cm^2)	119.6	60.6	158.5	290.2	682.3	222.7
R_s (ohm.cm^2)	512.7	571.0	81.3	488.4	620.3	791.7
Y_0 (µS*s$^\alpha$.cm^{-2})	100.4	91.0	66.9	36.2	74.8	58.7
α	0.765	0.795	0.802	0.845	0.736	0.781
Z(1mHz) (kohm.cm^2)	83 +/- 27	161 +/- 78	449 +/- 558	663 +/- 585	428 +/- 159	648 +/- 366

Table VII: Randles circuit fit parameters for the EIS spectra shown in Figure 13.

Alloy	**Ti-0**	**Ti-3.1**	**Ti-6.0**	**Ti-9.6**	**Ti-13.0**	**316L**
R_p (kohm.cm^2)	437.5	517.3	533.0	482.9	407.5	113.3
R_s (ohm.cm^2)	467.6	719.6	275.1	420.5	591.4	506.9
Y_0 (µS*s$^\alpha$.cm^{-2})	48.5	26.7	122.6	44.5	40.6	46.9
α	0.825	0.788	0.838	0.832	0.805	0.779
Z(1 mHz) (kohm.cm^2)	48 +/- 9	404 +/- 308	452 +/- 558	491 +/- 168	342 +/- 58	252 +/- 202

Table VIII: Surface cation fractions in atomic percent obtained via high-resolution XPS scans of the passive film formed following potentiostatic oxide growth (40 ks, -0.25 V_{SCE}) in 0.01 M NaCl. Surface cation fractions include intensities attributable to oxidized (non-zero valance) features normalized with relative sensitivity factors. Bolded terms are enriched relative to bulk composition.

Cation	0% Ti	6% Ti	9.6 % Ti
Al(III)	4.9%	**17.6%**	1.8%
Cr(III)	**69.0%**	**15.2%**	**50.8%**
Fe(II)/(III)	6.6%	9.7%	0.0%
Mn(II)	0.0%	0.1%	0.0%
Mo(VI)	**19.5%**	2.5%	**12.8%**
Ni(II)	0.0%	1.0%	0.0%
Ti(IV)	0.0%	**53.9%**	**34.5%**

Declaration of interests

- ☒ The authors declare that they have no known competing financial interests or personal relationships that could have appeared to influence the work reported in this paper.

Highlights

- The passivation and corrosion behavior of a Ti-containing, multi-phase complex concentrated alloy series is characterized.
- At increased Ti concentrations, an $L2_1$ phase enriched in Al, Ni, and Ti forms. At the highest evaluated Ti concentrations, a Laves phase enriched in Cr and Mo forms.
- Pitting and repassivation potentials increase with Ti content up to 6 at. % but decrease at higher Ti concentrations.
- Elemental fates are tracked with X-ray Photoelectron Spectroscopy and Atomic Emission Spectroelectrochemistry.

- Ti(IV) species are prevalent in the passive film despite Ti depletion in the FCC matrix.